AGU PUBLICATIONS

JGR

Journal of Geophysical Research: Solid Earth

RESEARCH ARTICLE
10.1002/2015JB012587

Key Points:
- Laboratory tests show that nonwelded interface model represents well the reflected waves from a fracture
- A new data-driven method to estimate heterogeneous fracture compliance from seismic reflections
- Numerical tests show that multiple reflections better estimate the compliance than primary reflections

Correspondence to:
S. Minato,
s.minato-1@tudelft.nl

Citation:
Minato, S., and R. Ghose (2016), Enhanced characterization of fracture compliance heterogeneity using multiple reflections and data-driven Green's function retrieval, *J. Geophys. Res. Solid Earth*, *121*, 2813–2836, doi:10.1002/2015JB012587.

Received 7 OCT 2015
Accepted 2 APR 2016
Accepted article online 9 APR 2016
Published online 30 APR 2016

©2016. The Authors.
This is an open access article under the terms of the Creative Commons Attribution-NonCommercial-NoDerivs License, which permits use and distribution in any medium, provided the original work is properly cited, the use is non-commercial and no modifications or adaptations are made.

Enhanced characterization of fracture compliance heterogeneity using multiple reflections and data-driven Green's function retrieval

Shohei Minato[1] and Ranajit Ghose[1]

[1] Department of Civil Engineering and Geosciences, Delft University of Technology, Delft, Netherlands

Abstract The spatial heterogeneity along a fracture is a key determinant for fracture-associated mechanical and hydraulic properties of the subsurface. Laboratory experiments have been performed to test the applicability of the nonwelded interface representation to predict the frequency- and angle-dependent elastic response of a single fracture. The observation that nonwelded interface model can represent quite well the frequency- and angle-dependent reflection response of a fracture has led us to develop a new methodology for estimating the spatially heterogeneous fracture compliance from the reflection response along a fracture surface. A data-driven approach based on Marchenko equation coupled with inverse scattering to solve the nonwelded interface boundary condition has been formulated. The approach estimates the elastic wavefield along a fracture accurately, including the multiple reflections. As an extension, it offers the possibility to estimate fracture compliance using the multiple reflections. We illustrate the concept by numerically modeling 2-D *SH* waves sensing the heterogeneous tangential compliance of a fracture. The stationary phase method is applied to single and double spatial integrals to analyze the effect of source and receiver aperture on the Green's function retrieval. Our results show that the use of multiple reflections allows a better estimation of the heterogeneous fracture compliance than using primary reflections alone, especially for the far offsets on the fracture plane.

1. Introduction

Fractures are ubiquitous in solid materials including Earth materials. Small-scale fractures like cracks and large-scale fractures like joints and faults are key structures that determine the mechanical resistance and the fluid transport properties of rocks. The mechanical properties of a fracture are described by its elastic compliances, which are primarily controlled by the surface roughness (asperity distribution) and the aperture of the fracture [e.g., *Brown and Scholz*, 1985; *Cook*, 1992]. Furthermore, studies in the past have illustrated the link of fracture compliances to stress field and fluid flow properties [e.g., *Hopkins et al.*, 1987; *Pyrak-Nolte and Morris*, 2000]. Characterizing fracture compliances is, therefore, crucial in addressing the mechanical, hydraulic, and transport properties of a fractured subsurface.

Although earlier studies characterized fractured reservoirs considering the elastic compliance of a fracture to be spatially homogeneous, the spatially varying nature of the fracture compliance was observed previously in laboratory experiments [*Pyrak-Nolte and Nolte*, 1992]. *Oliger et al.* [2003] and *Acosta-Colon et al.* [2009] also showed that mineral precipitation or stress distribution changes the local transmission response of elastic waves along a fracture plane, illustrating spatially varying nature of fracture compliances. Knowledge of the spatial variation of the elastic compliance of a fracture is important in order to determine the heterogeneous mechanical and hydraulic properties, e.g., evaluating the preferred fluid flow direction through the fracture or in the fractured medium.

Because seismic waves are sensitive to the mechanical properties of a fracture, seismically sensing and characterizing the fracture compliances is a promising approach [*Knight et al.*, 2010]. For this purpose, the nonwelded interface model or the linear-slip boundary representation for fractures [e.g., *Schoenberg*, 1980; *Baik and Thompson*, 1984; *Pyrak-Nolte et al.*, 1990] considers a fracture to be a thin soft layer. It is then effectively represented as an interface across which the seismic stress is continuous, but the displacement is

discontinuous, controlled by the fracture compliances. The boundary condition at a nonwelded interface is represented as,

$$[u_1] = \eta_T \tau_{13}, \tag{1}$$

$$[u_2] = \eta_T \tau_{23}, \tag{2}$$

$$[u_3] = \eta_N \tau_{33}, \tag{3}$$

where u_i and τ_{ij} are, respectively, the seismic displacement and the stress field in the Cartesian coordinates, the brackets indicates the jump or discontinuity across the fracture interface assumed here to be in $x_1 - x_2$ plane, and η_N and η_T are normal and tangential compliances, respectively.

The normal and tangential compliances are functions of the properties of the thin layer. *Baik and Thompson* [1984] approximated the seismic response of a thin, smooth welded layer by a nonwelded interface. *Hudson et al.* [1997] derived the normal and tangential compliances from the random distribution of asperity when the two rough fracture surfaces are coupled. These models can be written as follows [*Worthington and Lubbe*, 2007; *Choi et al.*, 2014]:

$$\eta_N^{-1} = r^w \frac{4\mu}{\pi a}\left(1 - \frac{V_S^2}{V_P^2}\right)\left(1 + \frac{2\,(r^w)^{1/2}}{\sqrt{\pi}}\right) + \frac{\lambda' + 2\mu'}{\Delta}, \tag{4}$$

$$\eta_T^{-1} = r^w \frac{8\mu}{\pi a}\left(1 - \frac{V_S^2}{V_P^2}\right)\left(1 + \frac{2\,(r^w)^{1/2}}{\sqrt{\pi}}\right) \Big/ \left(3 - \frac{2V_S^2}{V_P^2}\right) + \frac{\mu'}{\Delta}, \tag{5}$$

where V_P, V_S, and μ are, respectively, P wave velocity, S wave velocity, and the Lamé constant of the host material (rock without fracture), a is the mean radius of the contact areas (asperities), r^w is the proportion of the fracture surface area that is in contact, μ' and λ' are the Lamé constants of the fracture infill, and Δ is the mean aperture of the fracture. The first terms of equations (4) and (5) indicate the effect of the asperity distribution due to coupled rough surfaces, and the second terms indicate the effect of the thin, smooth welded layer. From these equations, one can see that estimation of the fracture compliances is useful for further understanding on asperity distribution, fracture aperture, and infill materials. The review of various fracture models using a nonwelded interface can be found in *Liu et al.* [2000].

In this study, we consider reflections from a nonwelded interface and also scattered waves due to the heterogeneity in compliance along the fracture. The assumption is that the elastic wavelength is larger than the thickness of the fracture and larger than the spacing between the asperities of contact, but the wavelength is shorter than the lateral extent of the fracture [*Gu et al.*, 1996; *Pyrak-Nolte and Morris*, 2000]. Although the nonwelded interface model has been extensively used in laboratory scale measurements [*Nagy*, 1992], the concept is highly general; any weak zone that is small with respect to the seismic wavelength can be characterized as a nonwelded interface. This representation should also be useful for in situ measurements of the compliances of large-scale fractures in the subsurface, e.g., joints and faults, as low-frequency seismic waves offer large wavelengths and long penetration distances. In this vein, the plane-wave reflection/transmission response of a nonwelded interface was studied earlier for rock joints [e.g., *Cook*, 1992; *Li et al.*, 2014] and macroscopic faults [e.g., *Worthington and Hudson*, 2000; *Kame et al.*, 2014].

In situ direct measurements of fracture compliances are sparse (see references in *Worthington and Lubbe* [2007]). *Worthington and Hudson* [2000] analyzed the anomalous attenuation (Q) observed in the vertical seismic profiling transmission response and discussed the viability of the nonwelded interface representation of geological faults. *Reshetnikov et al.* [2010] presented evidences that reflected seismic waves from a fracture were observed in the field where there was no lithological boundary predicted by logging data. However, there are no attempts made so far to characterize the spatial heterogeneity along the fractures. Recently, we proposed a new approach to estimate heterogeneous fracture compliances using the scattered waves measured at the Earth's surface, which is suitable for in situ evaluation [*Minato and Ghose*, 2013, 2014a]. The approach involves measurement of the spatial change of the scattered waves from a nonwelded interface (fracture) using a receiver array, extrapolating the wavefield at the fracture, and then solving the boundary condition to estimate the fracture compliance. This method involves two steps: (1) locating the position of

the fracture and (2) estimating the stress field along the fracture to solve the nonwelded-interface boundary condition. With a homogeneous background medium, it has been shown that the imaging (step 1) and the wavefield estimation along a fracture (step 2) are possible using the backpropagation of the reflection responses. However, for a more complex background medium a new methodology is required to handle accurately the effect of multiple reflections. To meet this need, a nonlinear imaging condition was earlier derived in order to image accurately the single and multiple fractures using multiply scattered waves [*Minato and Ghose*, 2014b, 2015].

Recently, *Wapenaar et al.* [2014a, 2014b] and *Broggini et al.* [2014] have presented a new method for retrieving the Green's function inside a medium using reflection responses at the surface of the Earth. The method solves the Marchenko equation and constructs the Green's function including the multiple reflections. We have made an extension of this method in order to characterize the heterogeneous fracture compliance, because this enables estimating the elastic wavefield along the fracture plane (step 2) accurately, handling the multiple reflections, without requiring the detailed subsurface information. Furthermore, it provides us with a possibility of characterizing the heterogeneous fracture compliance using the multiple reflections—in addition to the primary reflections, which is greatly advantageous but which has not been possible so far.

In this article, we first present the results of laboratory experiments to measure frequency- and angle-dependent seismic reflection responses of a simulated fracture and to examine the validity of the nonwelded interface representation. The frequency- and angle-dependent reflections will be used in estimating the spatially heterogeneous fracture compliances. Next, we briefly discuss the new data-driven Green's function retrieval approach and the use of inverse scattering to estimate the heterogeneous fracture compliances. We illustrate numerically the efficacy of this new approach. Finally, we examine the effect of source and receiver aperture on the Green's function retrieval by using the method of stationary phase. In the sections of data-driven Green's function retrieval and the application to numerically modeled data, we consider 2-D *SH* wave because (1) in this case the elastic wavefield senses the tangential component of the fracture compliance (tangential compliance, η_T) and (2) the simple scalar wavefield offers the essential insights regarding this new concept.

2. Frequency- and Angle-Dependent Reflection Coefficient of a Fracture: Laboratory Tests of a Nonwelded Interface Model

Our goal is to develop an approach for in situ characterization of heterogeneous fracture compliance in the Earth making use of frequency- and angle-dependent reflection responses of a nonwelded interface. Despite its broad implication, the concept of angle-dependent reflections from a nonwelded interface is not yet well utilized in order to characterize fracture compliances. The majority of laboratory experiments so far have used normal-incident seismic waves. The nonwelded interface model is applied to macroscopic faults, but only normal incident waves are considered [*Worthington and Hudson*, 2000; *Kame et al.*, 2014]. A few earlier studies that have considered oblique incidence are especially for nondestructive material testing [e.g., *Margetan et al.*, 1988; *Liaptsis et al.*, 2006; *Nam et al.*, 2012] and not for fractured rock characterization.

In this section, we shall investigate the frequency- and angle-dependent reflection coefficients and the efficacy of the nonwelded interface model through laboratory experiments. It will also show the advantage of using the nonwelded interface model: the measurement using a large seismic wavelength can handle correctly the frequency- and angle-dependent reflections from a thin, soft layer. We consider here *P* wave reflection due to *P* wave incidence.

Figure 1 illustrates our experimental setup consisting of two aluminum blocks with parallel and smooth surfaces (V_P = 6380 m/s, V_S = 3150 m/s, and ρ = 2700 kg/m^3). An artificial horizontal fracture is simulated by installing spacers (copper foils) of known thicknesses between the two blocks. We use four longitudinal transducers (Panametrics V103) for an array measurement (one transmitter and three receivers). The source-receiver offsets are 3.5, 7.0, and 10.5 cm, which provide the incident angles at the fracture (θ) of 5.8°, 11.5° and 17.0°, respectively. The central frequency of the source signal is 1 MHz. Figures 2a–2c show the measured reflection responses (PP reflection) from 100 μm thick fracture for dry condition (air-filled) and wet condition (fracture is filled with the mixture of water and hair gel). One can see the notable difference between the dry and wet conditions.

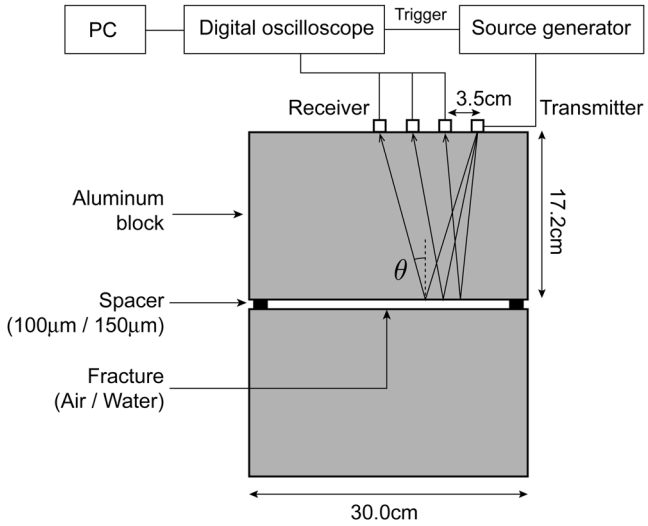

Figure 1. Experimental setup for measuring angle-dependent reflections from a fracture.

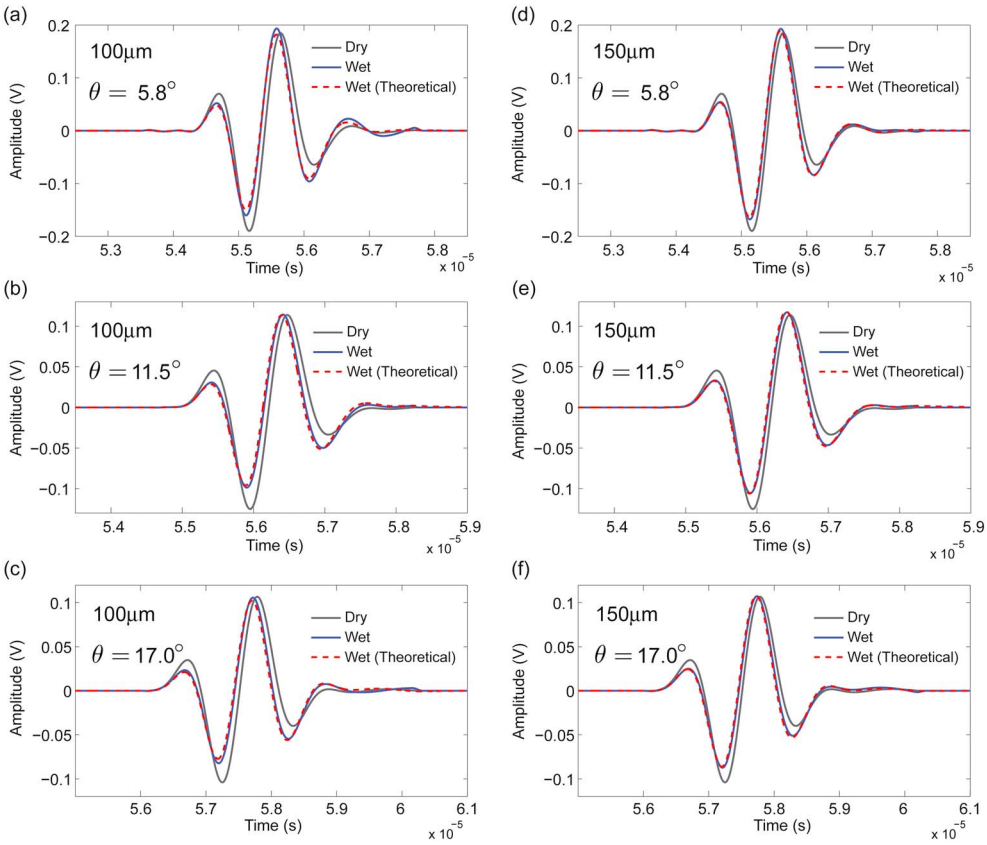

Figure 2. Observed reflection amplitudes from a simulated fracture under dry (air-filled) and wet (water-filled) condition. Three incident angles are considered for (a–c) 100 μm thick fracture and (d–f) 150 μm thick fracture. The nonwelded interface model predicts the theoretical response of the wet fracture assuming the normal compliance to be $\eta_N = 4.55 \times 10^{-14}$ m/Pa for Figures 2a–2c, and $\eta_N = 6.82 \times 10^{-14}$ m/Pa for Figures 2d–2f.

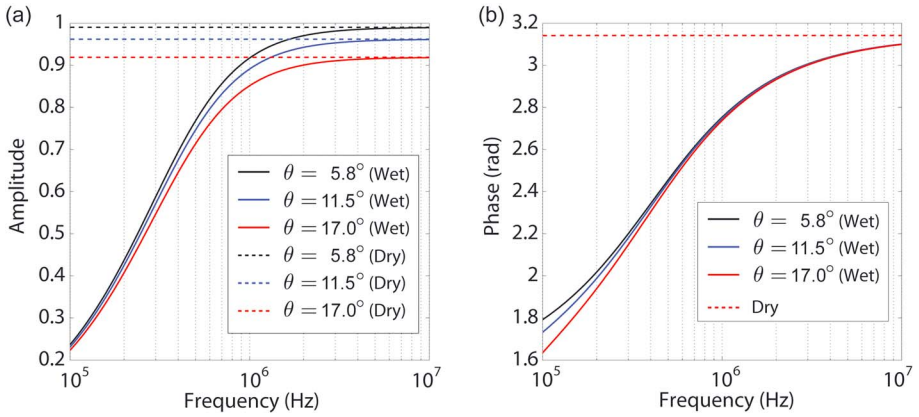

Figure 3. Theoretical reflection coefficients for 100 μm thick wet fracture ($\eta_N = 4.55 \times 10^{-14}$ m/Pa) and dry fracture ($\eta_N = 7.04 \times 10^{-10}$ m/Pa) for three angles of incidence.

The fracture in this experiment can be considered as a thin layer, with parallel boundaries, filled with a fluid. We assume the fracture compliance to be spatially invariant. In this case, the normal compliance (η_N) of the nonwelded interface is described by the second term in equations (4) and (5), which predicts η_N of the wet fracture and the dry fracture to be 4.55×10^{-14} m/Pa (using the value of the bulk modulus of water as 2.2×10^9 Pa) and 7.04×10^{-10} m/Pa (with the bulk modulus of air as 1.42×10^5 Pa), respectively. Note that the tangential compliance (η_T) is infinitely large due to the vanishingly small shear modulus of fluids. In Appendix A, we show the theoretical reflection coefficients of a nonwelded interface (equation (A1)). The theoretical values of the frequency- and angle-dependent reflection coefficients are calculated for different incidence angles (Figure 3) using the values of the normal compliance (η_N) of dry and wet fractures. One can see that the reflection coefficients are complex-valued functions of angle and frequency, which also causes a phase difference between incident and reflected waves. Note that due to the very large value of the normal compliance for a dry fracture (four order larger than that of a wet fracture), the dry fracture shows the highest frequency limit, i.e., it is sensed as a free surface whose reflection coefficients are not frequency dependent, and the reflection has an opposite polarity compared to the incident wave.

We use the reflection responses of the dry fracture (D^{Dry}) as a reference, and we predict the reflection responses of the wet fracture (D^{Wet}) using the following relation in the frequency domain:

$$D^{\text{Wet}} = \frac{R_{PP}^{\text{Wet}}}{R_{PP}^{\text{Dry}}} D^{\text{Dry}}, \tag{6}$$

where R_{PP}^{Wet} and R_{PP}^{Dry} are, respectively, the reflection coefficients (equation (A1)) of the wet fracture and the dry fracture (Figure 3). In this way, we mitigate the error due to the source directivity and the difference in receiver coupling. One can see that the nonwelded interface representation is remarkably accurate to predict the frequency- and angle-dependent reflection responses of a wet fracture (red lines in Figures 2a–2c). It also shows that through nonwelded interface representation, a large seismic wavelength (approximately 6.3 mm in this experiment) can correctly handle the reflection responses of a thin (100 μm) soft layer. Figures 2d–2f show the reflection responses from a thicker (150 μm) fracture. One can see that the reflection amplitude and phase of the wet fracture are different from those for the 100 μm thick fracture. Again, the nonwelded interface representation ($\eta_N = 6.82 \times 10^{-14}$ m/Pa) predicts the response very accurately. This laboratory validation justifies solving the linear-slip boundary condition for the frequency- and angle-dependent elastic wavefield along the fracture plane by a new approach, which will be discussed in the next section.

3. Theory

In this section, we will develop a new approach to characterize the heterogeneous fracture compliance using primary and multiple reflections, without using the detailed knowledge of the subsurface structure between the measurement surface and the fracture plane. We first illustrate the data-driven Green's function retrieval, and next we show the inverse scattering approach to characterize the heterogeneous fracture using the retrieved Green's functions.

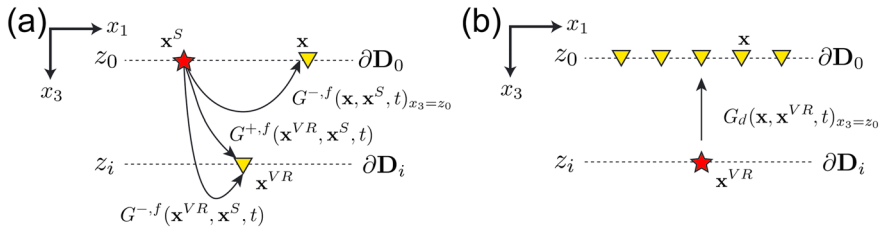

Figure 4. Configuration for data-driven Green's function retrieval. (a) We retrieve virtual receiver responses at $\partial\mathbf{D}_i$, i.e., $G^{\pm,f}(\mathbf{x}^{\mathrm{VR}},\mathbf{x}^{\mathrm{S}},t)$, from the reflection responses R and the (b) direct Green's function G_d. Note that R is a function of the upgoing Green's function at the surface $G^{-,f}(\mathbf{x},\mathbf{x}^{\mathrm{S}},t)_{x_3=z_0}$, see the main text. The Green's functions are retrieved as decomposed upgoing (−) and downgoing (+) functions. The Green's functions in Figure 4a are derived from true medium (without free surface), and they contain multiple reflections due to the heterogeneity in the medium, whereas the direct Green's function in Figure 4b can be estimated assuming the smoothed model.

3.1. Data-Driven Green's Function Retrieval

The goal is to extrapolate the scattering response measured at the surface down in depth to the fracture plane, without using the detailed subsurface information. Here we extrapolate the scattering response by creating new wavefield as if the virtual receivers are located right on the heterogeneous fracture. We assume that the location of the fracture is known a priori. This can be possible through dedicated seismic imaging, e.g., migration of reflected waves [e.g., *Nihei et al.*, 2000; *Reshetnikov et al.*, 2010; *Minato and Ghose*, 2014a, 2015]. Furthermore, the reflection response is assumed to be without free-surface-related multiple reflections. This can be achieved by preprocessing the data using, for example, the surface-related-multiple-elimination technique [*Verschuur et al.*, 1992].

The approach of data-driven Green's function retrieval is discussed next. The 3-D approach for acoustic media was derived using reciprocity theorems for one-way acoustic wavefield [e.g., *Wapenaar et al.*, 2014a, 2014b]. Assuming that the initial estimates of direct wavefields are given and ignoring the horizontally propagating waves, they show that the one-way (upgoing and downgoing) Green's functions from any position in the medium can be retrieved using only reflection responses measured at the surface. More importantly, the method will also correctly extrapolate the multiple reflections. The procedure is an iterative one involving the estimation of the upgoing and downgoing parts of the so-called focusing function which focuses at the virtual receiver position [e.g., *Wapenaar et al.*, 2014a]. The approach uses an estimate of the direct wavefield as the initial focusing function and then successively applies multidimensional crosscorrelation, time reversal and time-dependent muting to the initial focusing function and the reflection responses. The details concerning the physical interpretation of this iteration procedure are discussed earlier extensively [e.g., *Wapenaar et al.*, 2014b; *van der Neut et al.*, 2015].

We have used one-way 2-D *SH* wavefields [e.g., *Wapenaar et al.*, 2008] and modified the 3-D approach for acoustic media to 2-D *SH* wave configuration. In Appendix B, we present the detailed iteration procedure to estimate the Green's functions. Here we briefly show how we retrieve the wavefield. Figure 4 shows the 2-D configuration of the approach indicating $\mathbf{x} = (x_1, x_3)$ points a position vector in $x_1 - x_3$ plane. The two-way Green's function $G^{v_2,f}$ is defined as a particle velocity in x_2 direction (v_2) due to a point force in x_2 direction (f). The upgoing and downgoing Green's functions recorded at a virtual receiver on the fracture will be estimated for a source located at the measurement surface, i.e., $G^{\pm,f}(\mathbf{x}^{\mathrm{VR}},\mathbf{x}^{\mathrm{S}},t)$ using only the reflection response recorded at the measurement surface $G^{-,f}(\mathbf{x},\mathbf{x}^{\mathrm{S}},t)_{x_3=z_0}$ (Figure 4a). Here the superscripts VR and S indicate "Virtual Receiver" and "Source," respectively.

We first estimate the direct Green's function $G_d(\mathbf{x},\mathbf{x}^{\mathrm{VR}},t)_{x_3=z_0}$ due to the source located inside of the medium, which will be at the position of the virtual receiver (Figure 4b). We estimate the direct Green's function G_d using smoothed velocity and density models. We also estimate the travel time of the first arrivals between $\mathbf{x}^{\mathrm{VR}}$ and $\mathbf{x}$ at the surface as $t_d(\mathbf{x}^{\mathrm{VR}},\mathbf{x}_0)$ which can be obtained from the first arrivals of G_d. We then use the reflection response (R), the estimated direct Green's function (G_d) as the initial estimates of the focusing function, and the travel time of the first arrival t_d to iteratively update the focusing functions (see equations (B1)–(B3) in Appendix B). Here we consider velocity-normalized one-way wavefields, which corresponds to pressure-normalized one-way wavefields in acoustic media [*Wapenaar et al.*, 2014a]. Therefore, the reflection response R is defined as $R(\mathbf{x}^{\mathrm{S}},\mathbf{x}_0,\omega) = (1/2j\omega\mu^{-1})^{-1}\partial_{x_3}G^{-,f}(\mathbf{x},\mathbf{x}^{\mathrm{S}},\omega)_{x_3=z_0}$. Furthermore, the upgoing and downgoing Green's functions are related to the two-way Green's function as $G^{v_2,f} = G^{+,f} + G^{-,f}$.

Once the convergence is achieved through iterations (equations (B1) and (B2)), we then construct finally the up- and downgoing Green's function at the virtual receiver position $G^{\pm,f}(\mathbf{x}^{VR}, \mathbf{x}^{S}, t)$ using the estimated focusing functions (equations (B5) and (B6)).

Note that the retrieved Green's functions are biased by the transmission coefficients of the input direct Green's function [e.g., *Broggini et al.*, 2014]. We calculate the direct Green's function (G_d) right on the fracture without considering the nonwelded interface. This implies that we retrieve upgoing and downgoing Green's functions right *above* the fracture plane (see also Appendix D).

3.2. Heterogeneous Compliance Estimation Using Scattered Wave

Having retrieved the virtual receiver responses at positions $\mathbf{x}^{VR}$ right above the fracture plane, we can then estimate the heterogeneous fracture compliance by directly using the method presented in *Minato and Ghose* [2013, 2014a]. These earlier studies consider only primary reflections in a homogeneous medium. However, the formulation there is still valid for multiply reflected waves as long as the radiation condition in the bottom layer is sufficient. Characterization using multiple reflections is now possible because the Green's function retrieved using the Marchenko approach (previous section) correctly includes those multiple reflections. Here we adapt the formulation of full elastic waves [*Minato and Ghose*, 2013, 2014a] for the 2-D *SH* wavefield (see Appendix C for details).

The retrieved Green's function $G^{\pm,f}$ from equations (B5) and (B6) is in the form of particle velocity v_2. We can estimate corresponding stress field as

$$\tilde{\tau}_{23}^{\pm}(\omega, k_x) = \mp \frac{\mu k_{z,s}}{\omega} \tilde{v}_2^{\pm}(\omega, k_x), \tag{7}$$

where $k_{z,s} = \sqrt{(\omega/V_S)^2 - k_x^2}$ and $\Im(k_{z,s}) \leq 0$. Once the stress field along the fracture plane is estimated, one can estimate the heterogeneous compliance distribution. This requires solving the linear-slip boundary condition as represented in the frequency-wave number domain (equation (C4) in Appendix C), assuming that there is no upgoing wave in the lower medium:

$$\tilde{A}(\omega, k_x) = j\omega \eta_T(k_x) * \tilde{B}(\omega, k_x), \tag{8}$$

where $*$ denotes convolution in the wave number domain. The function $\tilde{A}$ and $\tilde{B}$ are calculated from the stress field at the fracture as

$$\tilde{A} = -\frac{2\omega}{\mu k_{z,s}} \tilde{\tau}_{23}^{-}, \tag{9}$$

$$\tilde{B} = \tilde{\tau}_{23}^{-} + \tilde{\tau}_{23}^{+}. \tag{10}$$

After inverse spatial Fourier transformation of equation (8), we obtain the heterogeneous compliance distribution as,

$$\eta_T(x) = \frac{\hat{A}(\omega, x)}{j\omega \left(1 + \epsilon^{\text{reg}} / |\hat{B}(\omega, x)|\right) \hat{B}(\omega, x)}, \tag{11}$$

where ϵ^{reg} is a regularization factor to stabilize the solution.

4. Numerical Modeling Results

4.1. Subsurface Model

We consider a two-layered elastic medium in which the second (bottom) layer includes a single heterogeneous fracture (Figure 5). The source and receiver arrays are installed in the first layer. The two boundaries (the layer boundary and the fracture) create multiple reflections which impinge on the fracture multiple times. This simple model offers useful insights on the concept that we propose here.

The heterogeneous fracture is represented by a random variation assuming Gaussian power spectral density, PSD [*Minato and Ghose*, 2014c], for the tangential compliance along a large fracture with a length of 1000 m. The average value of the tangential compliance is 1×10^{-9} (m/Pa). This order of magnitude for the tangential compliance was suggested while evaluating faults on field seismic data at a single borehole [*Worthington and Hudson*, 2000]. The compliance value changes along the fracture plane from 0.8×10^{-10} to 2.3×10^{-9}.

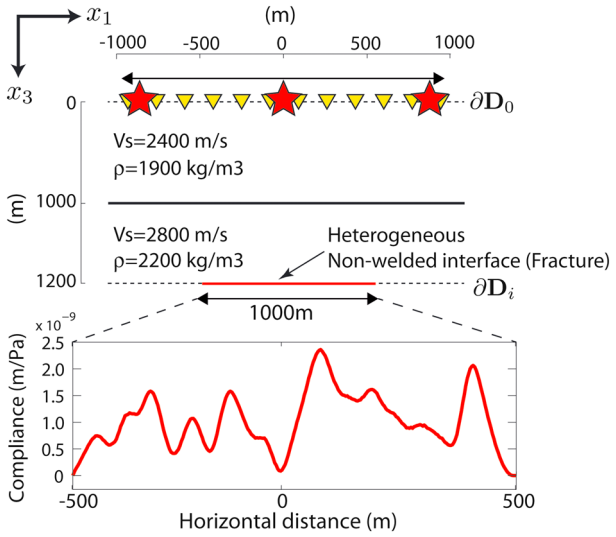

Figure 5. A two-layered subsurface, with a fracture located in the second (bottom) layer. A 1000 m long fracture with a spatially heterogeneous tangential compliance distribution is considered. The source and receiver arrays are located at the surface ($\partial\mathbf{D}_0$).

The edge of the fracture compliance is tapered to zero indicating completely welded interface. The following three models explain the variation of the tangential compliance:

1. *Thin welded layer model (second term in equation (5))*. When the fracture is made of a thin welded layer of a soft material, the variation of the thickness and/or the shear modulus of the filling material gives the spatial change in fracture compliance. For example, the inclusion of a 18 cm thick soil layer ($V_S = 300$ m/s and $\rho = 2000$ kg/m^3) gives the average value of η_T (1×10^{-9} m/Pa) and a thickness change between 1.4 cm to 41 cm, or a change in shear wave velocity of the filling from 198 m/s to 1060 m/s corresponds to the assumed compliance variation shown in Figure 5.
2. *Random asperity model (first term in equation (5))*. When the fracture is filled with fluids, the contact areas at the fracture (i.e., asperities) play a major role in transmitting the shear energy. In this case, the variation of the contact area from 1% to 20% along the fracture plane, keeping the mean contact radius constant at 0.3 m (i.e., $a = 0.3$, $r^w = 0.01 - 0.2$ and V_P/V_S ratio is 1.7), gives the assumed compliance variation.
3. *A combination of (1) and (2), i.e., equation 5*.

Detecting these variations is, therefore, key to infer the spatial change of the asperity distribution and/or the infilling material.

The 451 point sources and 451 receivers are installed with a spacing of 4 m. We model the responses in the frequency-wave number domain using the wdSDD method [*Nakagawa et al.*, 2004], modified to include an extra layer. Figure 6a shows the modeled reflection responses R at receivers located at 60 m interval due to a source located at the center of the array. A Ricker wavelet of 40 Hz center frequency has been convolved. The primary arriving event is a reflection from the boundary of two elastic layers, i.e., from the welded interface. The second arriving event is a reflection from the heterogeneous fracture (nonwelded interface). The rapid fluctuation in the amplitude of the second reflection event over the receiver array that we notice in Figure 6a is due to heterogeneous fracture compliance. More multiple reflections between the welded and the nonwelded interfaces arrive later on.

4.2. Green's Function Retrieval

For data-driven Green's function retrieval, we require an estimate of the direct Green's function (G_d) due to the source located inside of the medium, which will be at the position of the virtual receiver (equations (B1) – (B3)). We calculate this using smoothed velocity and density models (Figure 6b). We do not need the detailed structure between the measurement surface and the fracture plane. More specifically, a smooth model can be used as long as the smoothing does not affect the kinematics of propagation with respect to that of a real medium [e.g., *Wapenaar et al.*, 2014a]. We considered a simple overburden model. A medium with highly complex overburden requires an accurate estimation of input G_d. The limitation of the data-driven Green's function retrieval

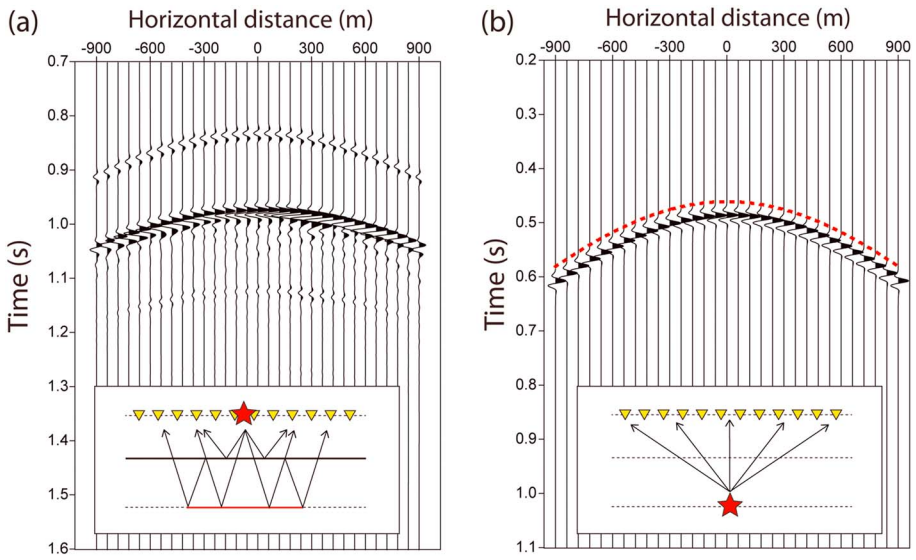

Figure 6. (a) Modeled reflection responses R at the measurement surface, with 60 m receiver spacing. (b) Direct waves G_d from a source at the virtual receiver modeled assuming a smoothed velocity and density model.

in case of a highly complex overburden and an alternative approach to estimate input G_d were studied earlier [e.g., *van der Neut et al.*, 2015; *Vasconcelos et al.*, 2015].

The dotted red line in Figure 6b shows the picked first arrivals used as $t_d^{\epsilon}(\mathbf{x}^{\mathrm{VR}}, \mathbf{x}_0)$ to design the muting function in the iteration procedure (equation (B4)). Figures 7a and 7b show the retrieved wavefield using the data-driven approach. The wavefield is retrieved as a common receiver gather, with the virtual receiver created at the center of the fracture (see Figures 7a and 7b (bottom) for source-receiver configuration). Note that only one iteration is sufficient for the convergence, for this simple model (see also Appendix D). The retrieved downgoing waves (Figure 7b) consist of the incident wave from the source at the Earth's surface and the multiple reflections which are incident on the fracture from above. The retrieved upgoing waves (Figure 7a) are the reflections from the heterogeneous fracture of the downgoing (incident and multiply reflected) waves. Therefore, these wavefields correspond to a situation when a virtual receiver is installed just above the fracture plane. The directly modeled results are overlain in Figures 7a and 7b. The method could retrieve the wavefield reasonably well, especially for the near-offset data. This can be seen in the difference gathers in Figures 7c and 7d. Retrieving the far-offset data requires a larger source-receiver aperture, as we will discuss in a later section.

Note that we calculate the difference gathers after applying a constant scaling factor to the retrieved wavefield. Our retrieved wavefield has amplitudes different from those in the direct modeling results, because the retrieved wavefield is biased by the transmission coefficient of the input direct wave (see Appendix D). One can see that this bias, however, will be canceled to some extent in the deconvolution procedure involved in the characterization method because of the same factor applied to both upgoing and downgoing waves (see Appendix D).

We repeat the procedure and create the virtual receivers at multiple positions along the fracture plane. Figure 8 is same as Figure 7, but for a common source gather with the source at the center of the array and the virtual receivers located along the fracture plane. As in the retrieved common receiver gather (Figure 7), the method could retrieve the wavefield well, especially at the near offsets. Figure 9 shows the retrieved traces at zero offset and at 400 m offset of Figures 8a and 8b. One can see that the downgoing waves are always better retrieved than the upgoing waves including the scattered waves (see second and later arriving events in Figures 9b and 9d). The far-offset traces are less accurate, especially for the upgoing wavefield (Figure 9c). These results are due to the effect of source and receiver apertures, which will be discussed in section 4.4.

It should be noted here that with this simple model the retrieval of upgoing waves is similar to the conventional extrapolation method [e.g., *Berkhout and Wapenaar*, 1993], as we need to execute only one iteration in the Green's function retrieval. This can be confirmed in equation (D23) (Appendix D), whereby the retrieval of upgoing wave is achieved by a simple extrapolation of the reflection responses R using the direct waves G_d as

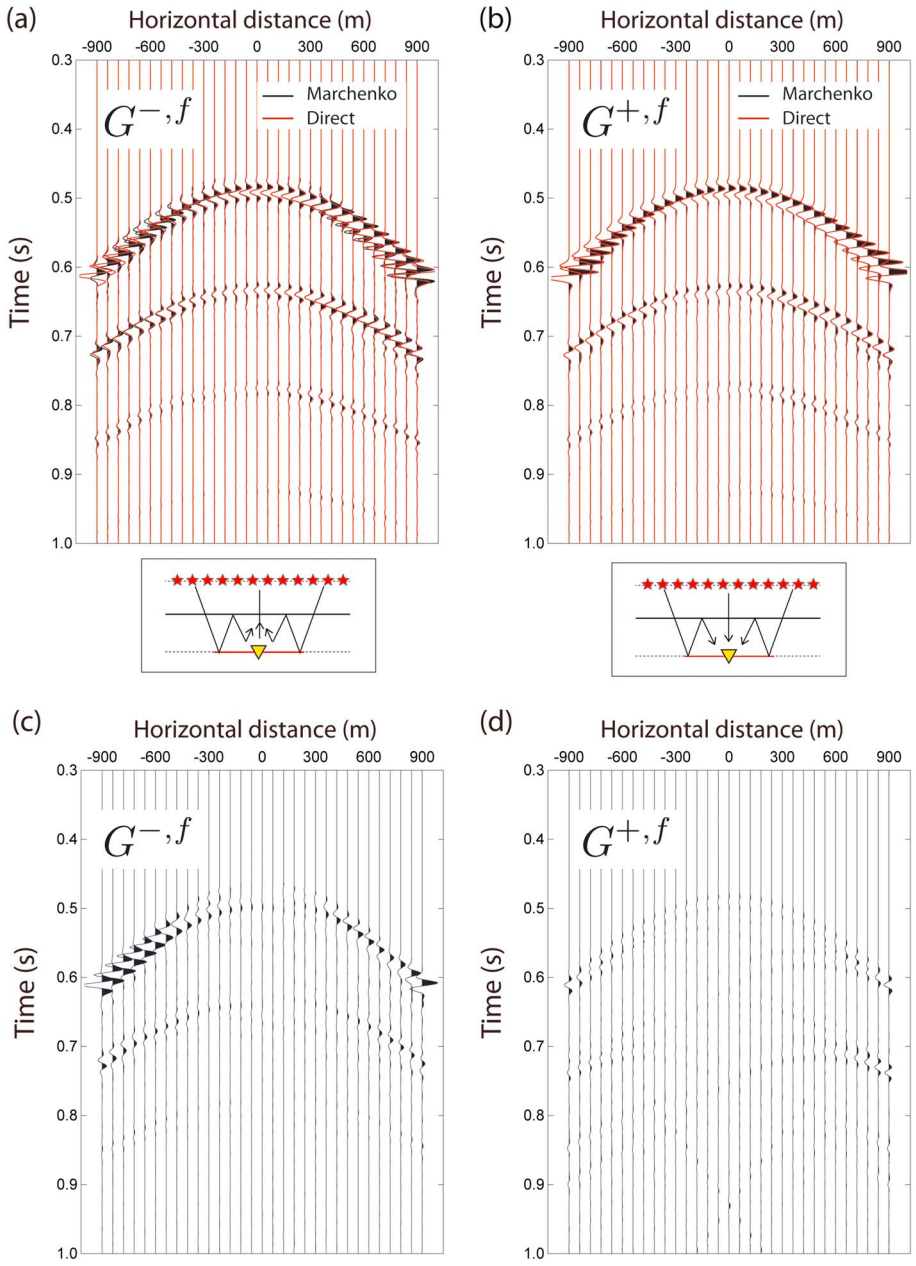

Figure 7. (a) Directly modeled and the retrieved upgoing Green's functions at a virtual receiver located right on the fracture plane. (b) Same as Figure 7a but for the downgoing Green's function. (c) The difference between directly modeled and the retrieved upgoing Green's functions. (d) Same as Figure 7c but for the downgoing Green's function. All plots are displayed with a time gain of t^7 applied to emphasize the later arrivals.

the extrapolation operators plus muting before first arrivals. However, our results clearly show that the *downgoing* waves are correctly retrieved, including multiple reflections and scattering (Figures 9b and 9d). This was not possible before with a conventional extrapolation method.

4.3. Compliance Estimation

We use the common-source gathers retrieved in the previous subsection (Figure 8) as input data for heterogeneous fracture characterization (equations (7)–(11)). Assuming that primary reflections and multiple reflections can be sufficiently separated in the time domain, the boundary condition (equation (8)) is locally satisfied for the primary reflections and the multiples. Therefore, we estimate heterogeneous fracture compliances separately using the primaries and the multiples with scattered waves which follow the reflections.

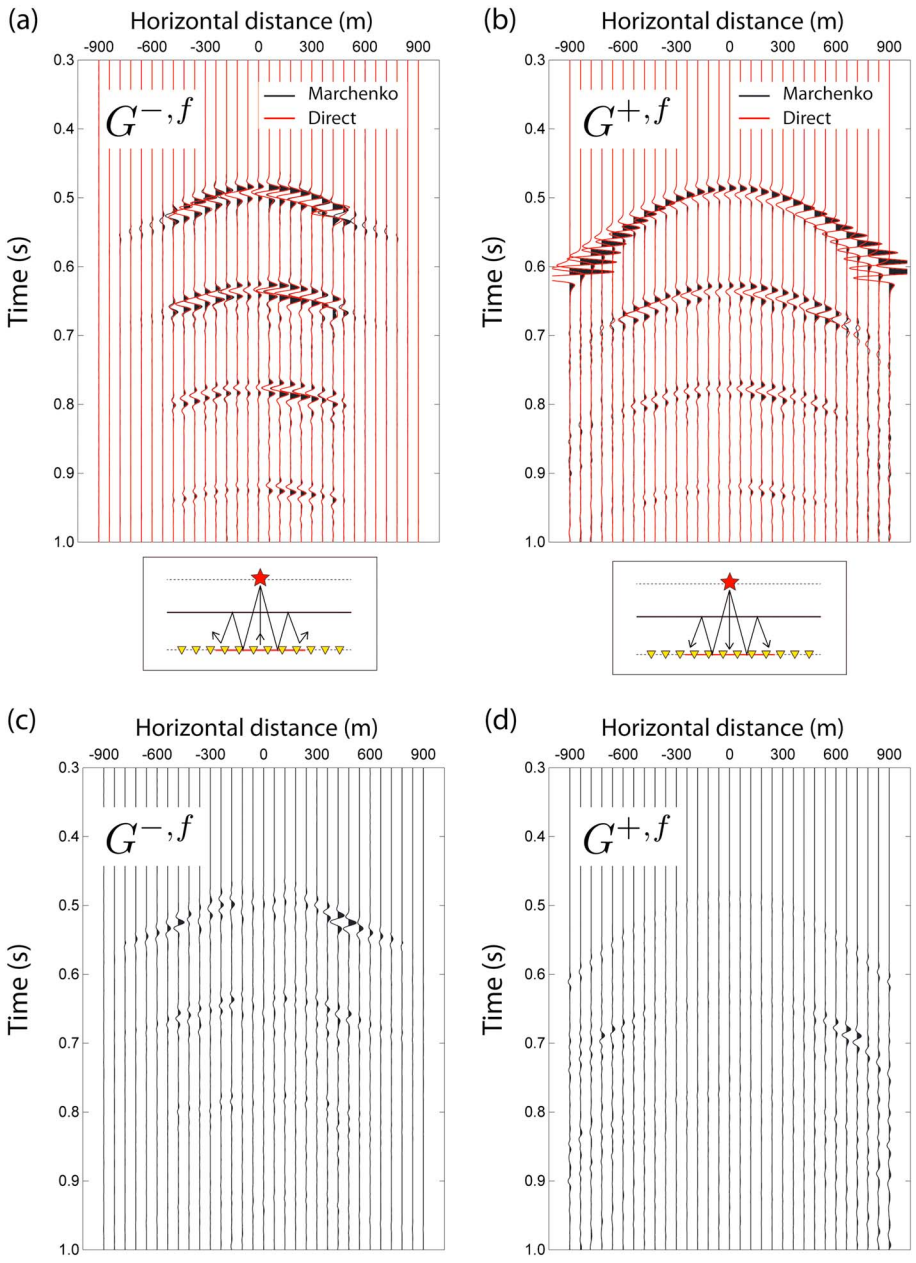

Figure 8. Same as Figures 7a and 7b but for a common source gather, after retrieving the virtual receiver responses at multiple positions on the fracture plane. All plots are displayed with a time gain of t^9.

We first use only the primary reflections and their scattered waves (windowing between the first arrivals and just before the secondary arriving events in Figure 8) to estimate the compliance distribution along the fracture plane. Because we solve the linear-slip boundary condition at each frequency, we can estimate the heterogeneous tangential compliance also at each frequency. Figure 10a shows this frequency-dependent variation. At the low frequency range (below 20 Hz), the estimated compliance is smooth and inaccurate. This is mainly because of the presence of the evanescent waves propagating along the fracture [e.g., *Pyrak-Nolte and Cook*, 1987], which are not correctly extrapolated by our approach. *Minato and Ghose* [2013, 2014a] discussed the effect of evanescent waves when using a conventional extrapolation operator. The high-angle scattered waves are also not correctly extrapolated due to the finite source-receiver aperture. The effect of the edge of the source and receiver arrays distorts the retrieved wavefield further. These may cause the observed variations with frequency. Note that the receiver spacing (spatial sampling) is also an important factor in

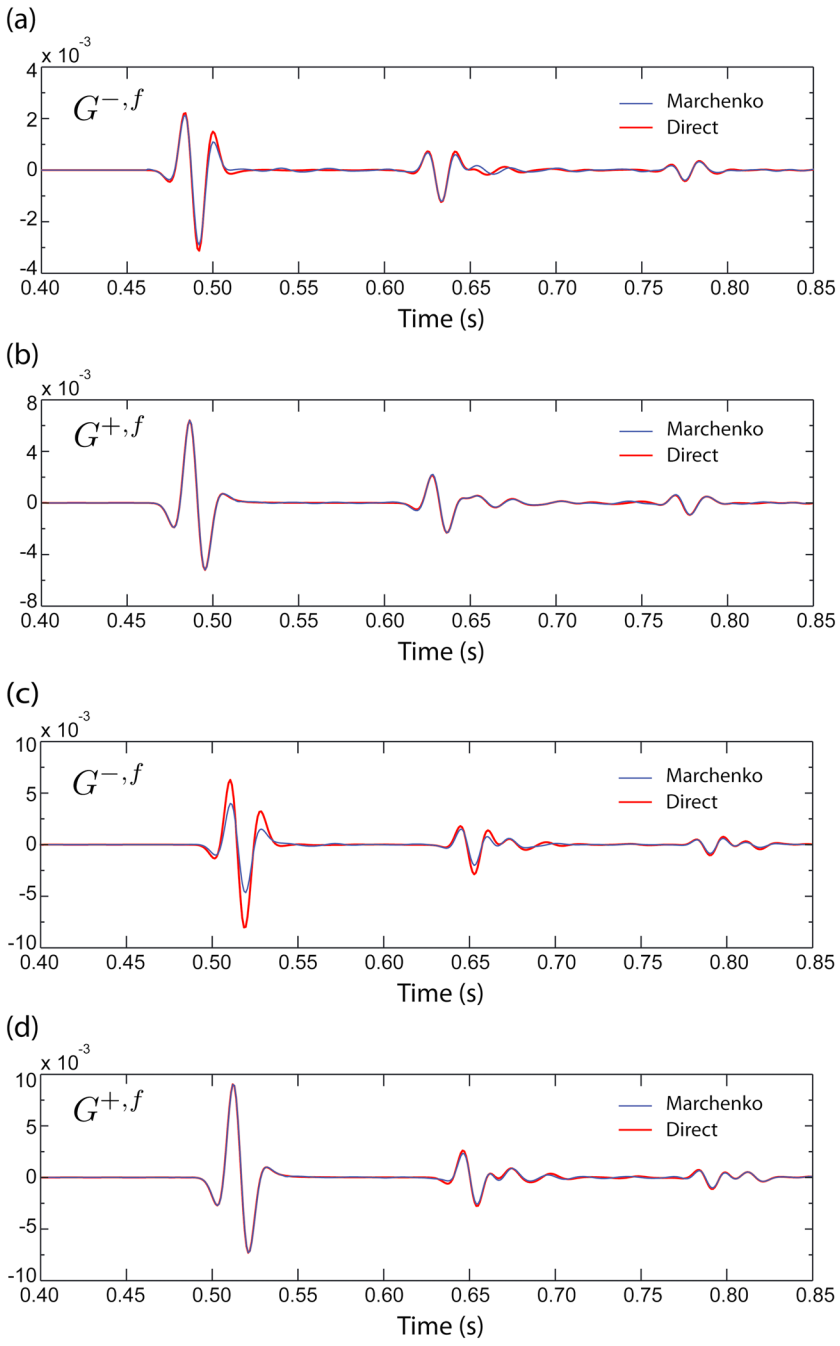

Figure 9. The Green's functions for the traces in Figure 8a and 8b. (a) Upgoing Green's function at zero offset and (b) downgoing Green's function at zero offset. (c and d) Same as Figures 9a and 9b but for the records at 400 m offset. All plots are displayed with a time gain of t^7.

estimating the heterogeneous compliances. *Minato and Ghose* [2013] showed that when the receiver sampling is not dense enough to capture the rapid variation of the wavefield, then the derived compliance distribution is rather smooth.

Figure 10b shows the estimated tangential compliance at 50 Hz. One can see that the retrieved primary reflection has estimated reasonably well the true compliance distribution, especially in the near offset. Next, we use only multiple reflections as input data (windowing all events including and below the secondary arriving events in Figure 8) to estimate the compliance distribution (Figure 10c). One can see that the compliance

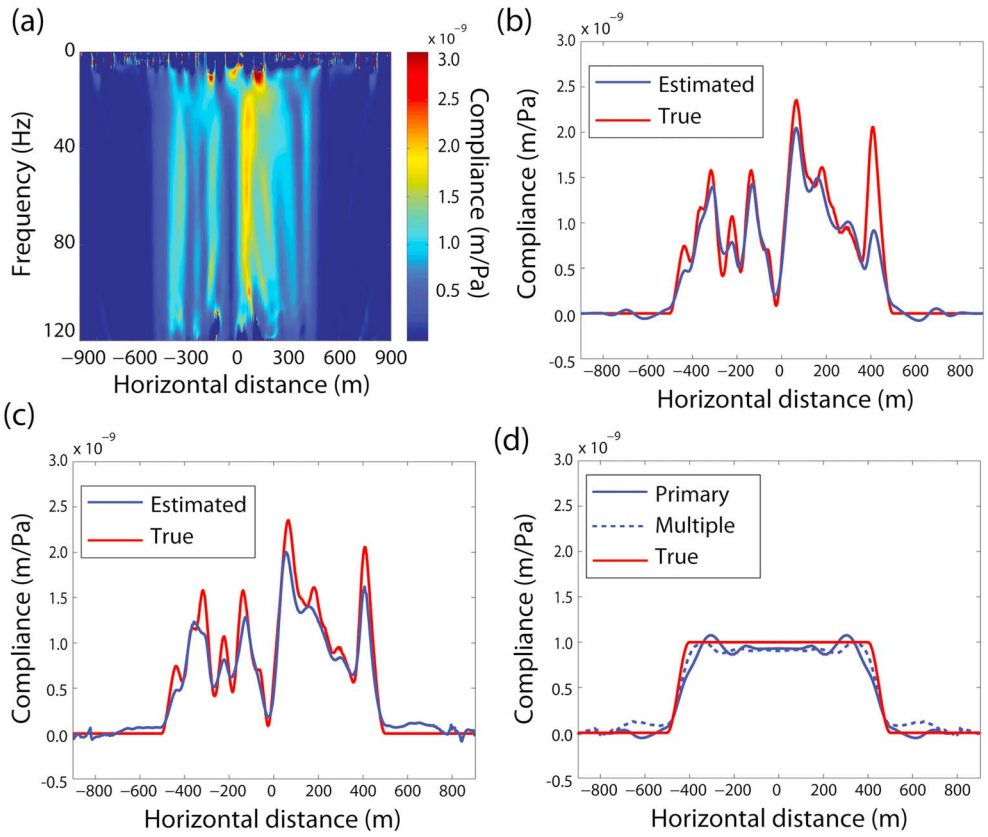

Figure 10. (a) Estimated tangential compliance using the retrieved primary reflections. (b) The result at 50 Hz in Figure 10a. (c) Same as Figure 10b but using the retrieved multiple reflections. (d) Estimated tangential compliance considering a simple compliance distribution, to illustrate the systematic differences.

value at 400 m is significantly better estimated than using the primary reflections alone. This is due to the source-receiver aperture limitation, which will be discussed in the next section.

In order to show more clearly the advantages of using multiple reflections, we repeated the same procedure described above, but considering a simple and laterally symmetric compliance distribution (Figure 10d). The estimated compliance values tend to be smaller than the true values. This is possibly because (a) the regularization required to stabilize the solution (equation (11)) affects the compliance values, (b) due to the effect of the edge of the source and receiver arrays distorting the retrieved wavefield, and (c) due to the high-angle scattering around the edge of the fracture being inaccurately extrapolated. However, it is clear that the estimated fracture compliance using the multiple reflections (dashed blue line in Figure 10d) is better than that obtained by using the primary reflections alone (solid blue line in Figure 10d), especially at the far offset. The result using the multiple reflections shows that the compliant zone along the fracture is longer than that estimated by the primary reflections.

4.4. Effect of Source and Receiver Apertures

We have illustrated that the data-driven Green's function retrieval provides the virtual receiver response in the subsurface including correctly the multiple (internal) reflections. We have also shown that using the retrieved upgoing and downgoing wavefields, the spatially heterogeneous fracture compliance can be estimated employing the inverse scattering approach. In this subsection, we discuss the effect of source and receiver apertures in the reflection data on the retrieval of upgoing and downgoing Green's functions.

In the first iteration ($k = 0$) of the retrieval process, the downgoing Green's function and the upgoing Green's function are represented by a double and a single spatial integral along the measurement surface, respectively (see equations (D1) and (D23)). From the method of stationary phase [e.g., *Chako*, 1965; *Conde et al.*, 2001], we find that the first iteration ($k = 0$) gives the correct total upgoing and downgoing Green's functions in our simple example (see Appendix D). We also find that due to the window function, there are limited

number of stationary phase pairs which contribute to the retrieved Green's functions. For example, the first-order multiple downgoing reflection (Figure D1a) is retrieved from the primary reflection from the second boundary (travel path of $\mathbf{x}^S \rightarrow z_2 \rightarrow \mathbf{x}^*$), the primary reflection from the first boundary ($\mathbf{x}^* \rightarrow z_1 \rightarrow \mathbf{y}^*$) and the direct wave ($\mathbf{y}^* \rightarrow \mathbf{x}^{VR}$), see Figure D3a. On the other hand, the corresponding first-order upgoing multiple reflection (Figure D1b) is retrieved from the first-order upgoing multiple reflection ($\mathbf{x}^S \rightarrow z_2 \rightarrow z_1 \rightarrow \mathbf{x}^{VR} \rightarrow \mathbf{x}^*$) and the direct wave ($\mathbf{x}^* \rightarrow \mathbf{x}^{VR}$), see Figure D5b. These interpretations imply that a larger source-receiver aperture is needed to retrieve the first-order multiple *upgoing* reflections than the first-order multiple downgoing reflections, because it is necessary to capture the first-order upgoing multiple reflections at the measurement surface (compare between Figure D3a and Figure D5b). This discussion holds true also for other type of reflections (e.g., primary and higher-order upgoing multiple reflections). The observation coincides with the fact that the retrieved upgoing wavefield (Figure 8a) is inferior to the downgoing wavefield (Figure 8b), especially at the far source-receiver offsets.

Next, we compare the retrieval of different orders of upgoing reflections from the fracture (second boundary). As one can see from Figures D5a and D5b, retrieving the primary reflections requires larger source-receiver offsets because the primary reflections in our model have larger incident angles, and we require larger source-receiver array to correctly capture them. On the other hand, the multiply reflected waves have smaller incident angles and require less array length than when using the primaries (compare Figure D5a and Figure D5b). This explains the result that the use of multiple reflections estimates better the fracture compliance at the far source-receiver offsets (Figures 10c and 10d).

Note that in this section and in Appendix D, we consider only specular reflections which obey the Snell's law. However, the scattering due to the spatial heterogeneity of the fracture compliance does not obey the Snell's law, and the stationary phase to retrieve the scattered wave obeys different rules. In fact, the stationary phase analysis for the scattered waves results in the stationary *lines* along the measurement surface which requires the observation to be made with an infinitely long receiver array. This is because of the requirement to capture the scattered energy which propagates in all directions from the scattering points, as shown in *van der Neut et al.* [2014, 2015] and similar discussion can be found in source-receiver interferometry [*Löer et al.*, 2014]. However, in the case of heterogeneous compliance distribution with a Gaussian PSD, the scattered energy is concentrated around the angle of the specular reflections [*Minato and Ghose*, 2014c]. Therefore, the stationary line around the stationary pairs for the (multiple) specular reflections may contribute more to retrieve scattered waves than other positions of the stationary line. This can explain the reason we have retrieved the scattered wave so well even with a finite source-receiver aperture, especially at the near offsets (Figure 7 and 8).

5. Conclusion

Nonwelded interface representation of a fracture provides an useful approach to characterize a thin, weak zone (e.g., fracture, joint, and fault) in the subsurface. The thickness can be much smaller than the wavelength. Such in situ estimation of heterogeneous fracture compliances is crucial to predict/evaluate fracture-associated mechanical, hydraulic, and transport properties in the subsurface. The results of our laboratory experiments establish that the frequency- and angle-dependent reflection responses from a single fracture can be estimated quite accurately using the nonwelded interface representation. This possibility is, therefore, exploited in the development of a characterization method for laterally heterogeneous fractures.

We have proposed a new method to characterize the heterogeneous fracture compliance using multiple reflections, by coupling the procedure with the data-driven Green's function retrieval. Two-dimensional numerical examples illustrate that the wavefield along the fracture plane is well retrieved except at the far offsets, without requiring the detailed structure/information between the measurement surface and the fracture plane. The method of stationary phase applied to a single and a double spatial integral in the data-driven Green's function retrieval shows that the retrieval of the multiple upgoing reflections requires less array length than that of the primary reflections. It also shows that retrieving the downgoing waves requires less array length than retrieving the upgoing waves. These arguments explain our observation that the use of retrieved multiple reflections leads to a better estimation of the heterogeneous fracture compliance than using primary reflections alone, especially at far offsets on the fracture plane.

We considered in this study a simple subsurface consisting of only two layers. However, the method is applicable to more complex multilayer Earth structures. In case of additional layers existing in the lower medium,

it will be necessary to window the target (multiple) reflections in order to ensure the radiation condition that is considered for estimating the heterogeneous compliance. In case of complex structures, furthermore, the accurate estimation of the initial direct wavefields and multiple iterations will be required in order to retrieve correctly the Green's functions [e.g., *Wapenaar et al.*, 2014a; *Vasconcelos et al.*, 2015]. We assumed that the position of the fracture is known using a priori processing, e.g., migration of the reflected waves. The error due to the inaccurate fracture location may be corrected in a data-driven manner by minimizing the imaginary components of the estimated compliance distribution, as illustrated in *Minato and Ghose* [2013]. Although we have considered 2-D *SH* wave in this study, the method should be equally useful for *P-SV* wave measurements, where the heterogeneous normal compliance can be estimated as well as the tangential compliance [*Minato and Ghose*, 2014a]. This can be achieved by using a data-driven Green's function retrieval approach modified for vector waves [e.g., *Wapenaar*, 2014; *Wapenaar and Slob*, 2014; *da Costa Filho et al.*, 2014, 2015].

Appendix A: Calculation of Reflection Coefficients in the Laboratory Experiments

We show here the theoretical PP reflection coefficient of a nonwelded interface in a homogeneous medium [*Chaisri and Krebes*, 2000]:

$$R_{PP} = \left[\omega^2 \eta_N \eta_T KL + 2i\omega\rho\eta\left(\eta_N \gamma^2 - \eta_T \chi^2 \xi^2\right)\right] D^{-1}, \tag{A1}$$

where,

$$D = \left(2\rho\xi - i\omega\eta_N K\right)\left(2\rho\eta - i\omega\eta_T K\right), \tag{A2}$$

$$\chi = 2\rho V_S^2 p, \gamma = \rho\left(1 - 2V_S^2 p^2\right), \tag{A3}$$

$$\xi = \frac{\cos\theta_{PP}}{V_P}, \eta = \frac{\cos\theta_{PS}}{V_S}, \tag{A4}$$

$$K = \gamma^2 + \chi^2 \xi\eta, L = \gamma^2 - \chi^2 \xi\eta. \tag{A5}$$

Here p is the ray parameter ($p = \sin\theta_{PP}/V_P$) and θ_{PP} and θ_{PS} are the angle of reflected P wave and S wave, respectively.

Appendix B: Data-Driven Green's Function Retrieval Using Marchenko Equation: 2-D SH Wave Configuration

We briefly show the data-driven Green's function retrieval using Marchenko equation in a 2-D *SH* wave configuration. Here we use the decomposed Marchenko equation in acoustic media [*Wapenaar et al.*, 2014b] and transform the field variables into those for a 2-D *SH* wave configuration.

The procedure is an iterative one, in order to estimate the upgoing and downgoing parts of the so-called focusing function ($f_1^{\pm}$ and its later arrivals M^+) which focuses at the virtual receiver position $\mathbf{x}^{\mathrm{VR}}$ on the fracture surface $\partial\mathbf{D}_i$ (Figure 4):

$$M_k^+\left(\mathbf{x}^S, \mathbf{x}^{\mathrm{VR}}, -t\right) = \int_{\partial\mathbf{D}_0} \mathrm{d}\mathbf{x}_0 \int_{-t_d^e\left(\mathbf{x}^{\mathrm{VR}}, \mathbf{x}_0\right)}^{t} R\left(\mathbf{x}^S, \mathbf{x}_0, t - t'\right) f_{1,k}^-\left(\mathbf{x}_0, \mathbf{x}^{\mathrm{VR}}, -t'\right) \mathrm{d}t', \tag{B1}$$

$$f_{1,k+1}^-\left(\mathbf{x}^S, \mathbf{x}^{\mathrm{VR}}, t\right) = f_{1,0}^-\left(\mathbf{x}^S, \mathbf{x}^{\mathrm{VR}}, t\right) + \int_{\partial\mathbf{D}_0} \mathrm{d}\mathbf{x}_0 \int_{-t_d^e\left(\mathbf{x}^{\mathrm{VR}}, \mathbf{x}_0\right)}^{t} R\left(\mathbf{x}^S, \mathbf{x}_0, t - t'\right) M_k^+\left(\mathbf{x}_0, \mathbf{x}^{\mathrm{VR}}, t'\right) \mathrm{d}t', \tag{B2}$$

$$f_{1,0}^-\left(\mathbf{x}^S, \mathbf{x}^{\mathrm{VR}}, t\right) = \int_{\partial\mathbf{D}_0} \mathrm{d}\mathbf{x}_0 \int_{-\infty}^{-t_d^e\left(\mathbf{x}^{\mathrm{VR}}, \mathbf{x}_0\right)} R\left(\mathbf{x}^S, \mathbf{x}_0, t - t'\right) T_d^{\mathrm{inv}}\left(\mathbf{x}^{\mathrm{VR}}, \mathbf{x}_0, t'\right) \mathrm{d}t', \tag{B3}$$

where the reflection responses R is defined as the responses with sources and receivers on the measurement surface $\partial\mathbf{D}_0$ (Figure 4), with $R(\mathbf{x}^S, \mathbf{x}_0, \omega) = (1/2j\omega\mu^{-1})^{-1}\partial_{x_3} G^{-,f}(\mathbf{x}, \mathbf{x}^S, \omega)_{x_3=z_0}$. We approximate the inverse of the transmission response T_d^{inv} to be its direct arrival; $T_d^{inv}(\mathbf{x}^{\mathrm{VR}}, \mathbf{x}_0, t) \approx G_d(\mathbf{x}, \mathbf{x}^{\mathrm{VR}}, -t)_{x_3=z_0}$. In order to derive equations (B1) to (B3), we use the causality of the Green's function and the focusing functions

[*Wapenaar et al.*, 2014b]. Therefore, the equations (B1)–(B3) are evaluated only for $t < t_d(\mathbf{x}^{VR}, \mathbf{x}^S)$, and we have the relation $M_k^+(\mathbf{x}^S, \mathbf{x}^{VR}, -t) = f_{1,k+1}^-(\mathbf{x}^S, \mathbf{x}^{VR}, t) = 0$ for $t \geq t_d(\mathbf{x}^{VR}, \mathbf{x}^S)$. Here $t_d(\mathbf{x}^{VR}, \mathbf{x}_0)$ is the travel time of first arrivals between $\mathbf{x}^{VR}$ and $\mathbf{x}$ at the surface. The travel time t_d^ϵ in equations (B1)–(B3) is used to design the muting function:

$$t_d^\epsilon = t_d - \epsilon, \tag{B4}$$

where ϵ is a small positive constant.

Once we estimate the focusing functions assuming that the iterations converge, we can retrieve the upgoing and downgoing Green's functions recorded at the virtual receiver ($\mathbf{x}^{VR}$) located inside the medium ($\partial\mathbf{D}_i$) from a source located on the measurement surface ($\partial\mathbf{D}_0$):

$$G^{+,f}\left(\mathbf{x}^{VR}, \mathbf{x}^S, t\right) = f_1^+\left(\mathbf{x}^S, \mathbf{x}^{VR}, -t\right) - \int_{\partial\mathbf{D}_0} d\mathbf{x}_0 \int_{-\infty}^{t} R\left(\mathbf{x}^S, \mathbf{x}_0, t-t'\right) f_1^-\left(\mathbf{x}_0, \mathbf{x}^{VR}, -t'\right) dt', \tag{B5}$$

$$G^{-,f}\left(\mathbf{x}^{VR}, \mathbf{x}^S, t\right) = -f_1^-\left(\mathbf{x}^S, \mathbf{x}^{VR}, t\right) + \int_{\partial\mathbf{D}_0} d\mathbf{x}_0 \int_{-\infty}^{t} R\left(\mathbf{x}^S, \mathbf{x}_0, t-t'\right) f_1^+\left(\mathbf{x}_0, \mathbf{x}^{VR}, t'\right) dt', \tag{B6}$$

where the focusing function f_1^+ can be constructed from its later arrivals as $f_{1,k}^+(\mathbf{x}^S, \mathbf{x}^{VR}, t) = T_d^{inv}(\mathbf{x}^{VR}, \mathbf{x}^S, t) + M_{k-1}^+(\mathbf{x}^S, \mathbf{x}^{VR}, t)$.

Appendix C: Heterogeneous Compliance Estimation Using Scattered Waves: 2-D SH Wave Configuration

The formulation of heterogeneous compliance estimation for full elastic wave is presented using the one-way wavefield equation [*Minato and Ghose*, 2013]. The one-way wavefield equation is derived by considering laterally invariant medium, representing the two-way wavefield equation in a matrix form and obtaining the eigenvector matrix of an operator matrix [e.g., *Woodhouse*, 1974; *Ursin*, 1983; *Wapenaar and Berkhout*, 1989]. The eigenvector matrix is then used to decompose the two-way wavefield into the one-way (upgoing and downgoing) wavefield.

The equation for one-way wavefield for 2-D *SH* waves can be obtained considering the acoustic case [e.g., *Wapenaar and Berkhout*, 1989] and transforming the field variables to those for 2-D *SH* wave. The comparison of the variables in the matrix operator between the acoustic formulation and the 2-D *SH* wave formulation can be found in, e.g., the Appendix B of *Wapenaar et al.* [2008]. In the frequency-wave number domain, the one-way wavefield equation is written as,

$$\begin{pmatrix} \tilde{v}_2 \\ -\tilde{\tau}_{23} \end{pmatrix} = \mathbf{L} \begin{pmatrix} \tilde{v}_2^+ \\ \tilde{v}_2^- \end{pmatrix}, \tag{C1}$$

where $\mathbf{L}$ is a composition matrix (eigenvector matrix) defined as

$$\mathbf{L} = \begin{pmatrix} 1 & 1 \\ \mu k_{z,s}/\omega & -\mu k_{z,s}/\omega \end{pmatrix}. \tag{C2}$$

In the frequency-wave number domain, the boundary condition of a nonwelded interface (equation (2)) can be written as,

$$\tilde{v}_{2,l}^+ = \tilde{v}_{2,u}^+ + \tilde{v}_{2,u}^- + i\omega\eta_T * \left(\tilde{\tau}_{23,u}^+ + \tilde{\tau}_{23,u}^-\right), \tag{C3}$$

here $*$ denotes convolution in the wave number domain and subscripts *u* and *l* indicate, respectively, that the quantities are at just above (upper medium) and below (lower medium) the interface. To derive equation (C3), we assume that there is no upgoing wave in the lower medium. This condition is useful for this study because in the data-driven Green's function retrieval, we retrieve wavefields just above the interface (i.e., $\tilde{v}_{2,u}^\pm$). Furthermore, we characterize the fracture compliance from the interaction between downgoing waves which impinge on the fracture ($\tilde{v}_{2,u}^+$ or $\tilde{\tau}_{23,u}^+$) and correspondingly generated upgoing waves ($\tilde{v}_{2,u}^-$ or $\tilde{\tau}_{23,u}^-$). When heterogeneity exists in the lower medium (e.g., additional layers), one can window the target (multiple) reflections in order to ensure the radiation condition.

The boundary condition (equation (C3)) are then represented by the stress field in the upper medium (i.e., $\tilde{\tau}^{\pm}_{23,u}$) using equations (C1), (C2), and (7):

$$-\frac{2\omega}{\mu k_{z,s}}\tilde{\tau}^{-}_{23,u} = j\omega\eta_T * \left(\tilde{\tau}^{+}_{23,u} + \tilde{\tau}^{-}_{23,u}\right), \tag{C4}$$

where we assume the same medium parameters for the upper and the lower media and we use the relation of the continuation of stress field ($\tilde{\tau}^{+}_{23,l} = \tilde{\tau}^{+}_{23,u} + \tilde{\tau}^{-}_{23,u}$).

Appendix D: Stationary Phase Analysis

D1. Downgoing Green's Function

We show here, using the stationary phase analysis, the effect of the source and receiver apertures on the retrieval of the Green's function. *Broggini et al.* [2014] showed the stationary phase analysis for an alternative expression of the data-driven Green's function retrieval, which results in a single spatial integral. We apply the method of stationary phase to equations (B5) and (B6), which results in a single and a double spatial integral, respectively. The method of stationary phase applied to equations (B5) and (B6) offers key insight on the effect of the source-receiver aperture on the retrieval of upgoing and downgoing Green's functions individually.

We assume a simple geometry of a horizontal source-receiver aperture and two boundaries in the subsurface. In the following analysis, we ignore the refraction effect at the boundary. However, our raypath discussion is also useful for more complex subsurface structures.

From equation (B5), the first iteration ($k = 0$) gives the retrieved downgoing Green's function as,

$$\hat{G}^{+,f}\left(\mathbf{x}^{\mathrm{VR}}, \mathbf{x}^{\mathrm{S}}, \omega\right) = \hat{G}_d\left(\mathbf{x}^{\mathrm{S}}, \mathbf{x}^{\mathrm{VR}}, \omega\right) - \iint_{\partial \mathbf{D}_0} \mathrm{d}\mathbf{x}_0 \mathrm{d}\mathbf{y}_0 \hat{R}\left(\mathbf{x}^{\mathrm{S}}, \mathbf{x}_0, \omega\right) \left[\hat{R}^{*}\left(\mathbf{x}_0, \mathbf{y}_0, \omega\right) \hat{G}_d\left(\mathbf{y}_0, \mathbf{x}^{\mathrm{VR}}, \omega\right)\right]_{w(\mathbf{x}_0, \mathbf{x}^{\mathrm{VR}}, t)}, \tag{D1}$$

where $\hat{}$ indicates that the quantities are considered in the frequency domain. The symbol $[\cdot]_{w_d(\mathbf{x}_0, \mathbf{x}^{\mathrm{VR}}, t)}$ means that the quantity inside the bracket is windowed in the time domain according to the window function $w_d(\mathbf{x}_0, \mathbf{x}^{\mathrm{VR}}, t)$, where $w_d(\mathbf{x}_0, \mathbf{x}^{\mathrm{VR}}, t) = 1$ for $t > -t^{e}_{d}(\mathbf{x}_0, \mathbf{x}^{\mathrm{VR}})$ and $w_d(\mathbf{x}_0, \mathbf{x}^{\mathrm{VR}}, t) = 0$ for $t \leq -t^{e}_{d}(\mathbf{x}_0, \mathbf{x}^{\mathrm{VR}})$. Note that $\mathbf{x}_0 = (x_1, x_3)_{x_3 = z_0}$ and $\mathbf{y}_0 = (y_1, y_3)_{y_3 = z_0}$ are on the measurement surface $\partial \mathbf{D}_0$.

We substitute the asymptotic Green's function for $\hat{G}_d$ and the reflection response on the measurement surface $\hat{R}$, assuming a simple two-layered model.

$$\hat{G}_d\left(\mathbf{x}^{\mathrm{S}}, \mathbf{x}^{\mathrm{VR}}, \omega\right) = \tau_d \mu^{-1}\left(\mathbf{x}^{\mathrm{VR}}\right) \hat{G}_0(r_d, \omega), \tag{D2}$$

$$\hat{G}_0(r_d, \omega) = j\omega \frac{\exp\left(-j\left(kr_d + \pi/4\right)\right)}{\sqrt{8\pi k r_d}}, \tag{D3}$$

$$r_d = \sqrt{\left(x^{\mathrm{VR}}_1 - x^{\mathrm{S}}_1\right)^2 + \left(x^{\mathrm{VR}}_3 - x^{\mathrm{S}}_3\right)^2}, \tag{D4}$$

where $k = \omega / V_S$ and τ_d indicates any transmission coefficient which is used to calculate G_d.

$$\hat{R}(\mathbf{x}, \mathbf{x}^{S}, \omega) = \sum_{n=1}^{\infty} \hat{R}^{(n)}(\mathbf{x}, \mathbf{x}^{S}, \omega), \tag{D5}$$

where

$$\hat{R}^{(n)}(\mathbf{x}, \mathbf{x}^{S}, \omega) = \frac{jkA^{(n)} z^{(n)}_0}{|\mathbf{x}^{(n)} - \mathbf{x}^{S}|} \frac{\exp\left(-j\left(k|\mathbf{x}^{(n)} - \mathbf{x}^{S}| + \pi/4\right)\right)}{\sqrt{2\pi k |\mathbf{x}^{(n)} - \mathbf{x}^{S}|}}, \tag{D6}$$

where $\mathbf{x}^{(n)}$ is the mirror image of $\mathbf{x}$ with respect to the boundaries [*Broggini et al.*, 2014]. For example, $\mathbf{x}^{(0)}$ is the mirror image of $\mathbf{x}$ with respect to the first boundary (which indicates the primary reflection from the first boundary), $\mathbf{x}^{(1)}$ is the mirror image with respect to the second boundary (the primary reflection from the second boundary), and $\mathbf{x}^{(2)}$ is the mirror image of $\mathbf{x}$ with respect to the first and second boundary (the first-order multiple reflection). $A^{(n)}$ indicates the amplitude coefficient for the nth reflection event, e.g., $A^{(0)} = r^{+}_1$, $A^{(1)} = \tau^{+}_1 r^{+}_2 \tau^{-}_1$ and $A^{(2)} = \tau^{+}_1 (r^{+}_2)^2 r^{-}_1 \tau^{-}_1$, where $r^{\pm}_{1,2}$ and $\tau^{\pm}_{1,2}$ are the reflection/transmission coefficients of the first/second boundary for the downgoing (+) / upgoing (−) wave, respectively.

Substituting equation (D2) and (D5) into equation (D1) gives,

$$\hat{G}^{+,f}(\mathbf{x}^{\mathrm{VR}},\mathbf{x}^{\mathrm{S}},\omega)=\tau_d\mu^{-1}(\mathbf{x}^{\mathrm{VR}})\left[\hat{G}_0(r_d,\omega)-\sum_{n=1}^{\infty}\sum_{m=0}^{\infty}F^{(n,m)}\exp\left(-j\pi/4\right)\right], \tag{D7}$$

where,

$$F^{(n,m)}=\iint_{-\infty}^{\infty}\mathrm{d}x_1\mathrm{d}y_1 f(x_1,y_1)\exp\left(-jk\phi(x_1,y_1)\right), \tag{D8}$$

$$f(x_1,y_1)=\frac{k\omega A^{(n)}A^{(m)}\left(x_3^{\mathrm{S}(n)}-x_3\right)\left(x_3^{(m)}-y_3\right)}{r_{xs}^{(n)\,3/2}r_{xy}^{(m)\,3/2}r_{yR}^{1/2}}\frac{j}{2\pi\sqrt{8\pi k}}, \tag{D9}$$

and

$$\phi(x_1,y_1)=r_{xs}^{(n)}-r_{xy}^{(m)}+r_{yR}, \tag{D10}$$

where $r_{xs}^{(n)}$, $r_{xy}^{(m)}$, and r_{yR} are functions of (x_1,y_1):

$$r_{xs}^{(n)}(x_1)=\sqrt{\left(x_1-x_1^{\mathrm{S}(n)}\right)^2+\left(x_3-x_3^{\mathrm{S}(n)}\right)^2}, \tag{D11}$$

$$r_{xy}^{(m)}(x_1,y_1)=\sqrt{\left(y_1-x_1^{(m)}\right)^2+\left(y_3-x_3^{(n)}\right)^2}=\sqrt{\left(x_1-y_1^{(m)}\right)^2+\left(x_3-y_3^{(n)}\right)^2}, \tag{D12}$$

$$r_{yR}=\sqrt{\left(y_1-x_1^{\mathrm{VR}}\right)^2+\left(y_3-x_3^{\mathrm{VR}}\right)^2}. \tag{D13}$$

Note that we consider the measurement surface to be at zero depth (i.e., $z_0=x_3=y_3=0$).

The stationary points x_1^*,y_1^* satisfy $\partial\phi/\partial x_1=\partial\phi/\partial y_1=0$. This relation can be written as,

$$\left(x_1^*-x_1^{\mathrm{S}}\right)r_{xs}^{(n)\,-1}=\left(x_1^*-y_1^*\right)r_{xy}^{(m)\,-1},$$

$$\left(y_1^*-x_1^{\mathrm{VR}}\right)r_{yR}{}^{-1}=\left(y_1^*-x_1^*\right)r_{xy}^{(m)\,-1}. \tag{D14}$$

Note further that we take into consideration the effect of the window function $w_d(\mathbf{x}_0,\mathbf{x}^{\mathrm{VR}},t)$ in equation (D1). This can be achieved by posing an additional constraint on the stationary phase pairs as,

$$r_{yR}+r_{xR}>r_{xy}^{(m)}, \tag{D15}$$

where,

$$r_{xR}=\sqrt{\left(x_1-x_1^{\mathrm{VR}}\right)^2+\left(x_3-x_3^{\mathrm{VR}}\right)^2}. \tag{D16}$$

The values of the second-order derivatives of ϕ at the stationary points become,

$$a=\left.\frac{\partial^2\phi}{\partial x_1^2}\right|_{x_1^*,y_1^*}=r_{xs}^{(n)\,-1}\left(1-\left(x_1^*-x_1^{\mathrm{S}}\right)^2r_{xs}^{(n)\,-2}\right)-r_{xy}^{(m)\,-1}\left(1-\left(x_1^*-y_1^*\right)^2r_{xy}^{(m)\,-2}\right), \tag{D17}$$

$$b=\left.\frac{\partial^2\phi}{\partial y_1^2}\right|_{x_1^*,y_1^*}=r_{yR}{}^{-1}\left(1-\left(y_1^*-x_1^{\mathrm{VR}}\right)^2r_{yR}{}^{-2}\right)-r_{xy}^{(m)\,-1}\left(1-\left(y_1^*-x_1^*\right)^2r_{xy}^{(m)\,-2}\right), \tag{D18}$$

$$c=\left.\frac{\partial^2\phi}{\partial x_1\partial y_1}\right|_{x_1^*,y_1^*}=-r_{xy}^{(m)\,-1}\left(1-\left(x_1^*-y_1^*\right)^2r_{xy}^{(n)\,-2}\right), \tag{D19}$$

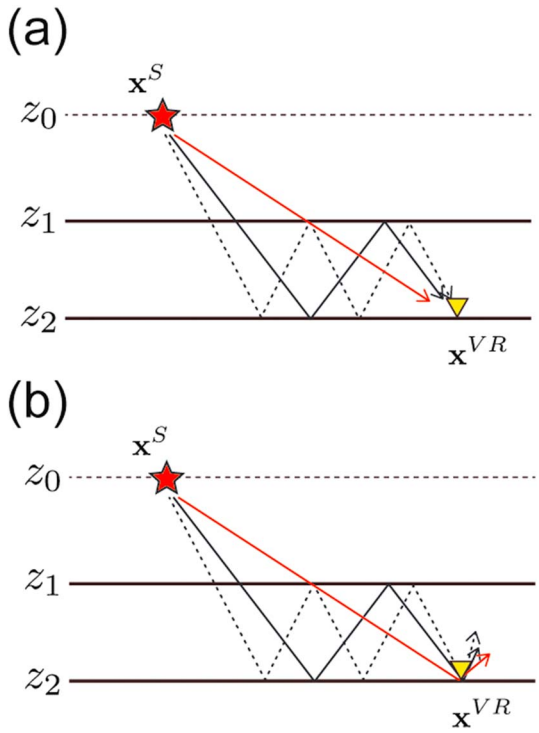

Figure D1. (a) Source-receiver configuration and configurations of downgoing direct wave (red line), first-order downgoing multiple reflection (black solid line), and second-order downgoing multiple reflection (dotted line). (b) The primary upgoing reflection, first- and second-order multiple upgoing reflections have the same travel paths as the downgoing waves in Figure D1a but multiplied with the corresponding reflection coefficients at the second boundary.

Assuming that the stationary phase pair (x_1^*, y_1^*) exists under the fixed values of m and n, the method of stationary phase for a double integral [e.g., *Chako*, 1965; *Conde et al.*, 2001] approximates the response of F (equation (D8)) as,

$$F^{(n,m)} \approx 2\pi f\left(x_1^*, y_1^*\right) \frac{\exp\left(-jk\phi\left(x_1^*, y_1^*\right)\right)}{k\sqrt{|ab-c^2|}} = j\omega A^{(n)} A^{(m)} \frac{\exp\left(-jk\phi\left(x_1^*, y_1^*\right)\right)}{\sqrt{8\pi k\phi\left(x_1^*, y_1^*\right)}}. \tag{D20}$$

Here we consider only the stationary phase pair which produces the causal response (i.e., $\phi > 0$).

Summation of contributions from all stationary phase pairs (x_1^*, y_1^*) from all possible combinations of multiple reflections (i.e., infinite number of m and n) in equation (D7) results in the retrieved upgoing Green's function as:

$$\hat{G}^{+,f}(\mathbf{x}^{\mathrm{VR}}, \mathbf{x}^{\mathrm{S}}, \omega) \approx \tau_d' j\omega\mu^{-1}(\mathbf{x}^{\mathrm{S}}) \left[\frac{\exp\left(-j\left(kr_d + \pi/4\right)\right)}{\sqrt{8\pi kr_d}} - \sum_{x_1^*, y_1^*} \frac{A^{(n)}A^{(m)}\exp\left(-j\left(k\phi\left(x_1^*, y_1^*\right) + \pi/4\right)\right)}{\sqrt{8\pi k\phi\left(x_1^*, y_1^*\right)}}\right], \tag{D21}$$

where $A^{(n)}$ and $A^{(m)}$ change with the stationary phase pairs and we redefine a transmission coefficient as $\tau_d' = \tau_d \mu(\mathbf{x}^S)\mu^{-1}(\mathbf{x}^{VR})$.

Downgoing direct wave. We check the retrieval of a downgoing direct wave (travel path of $\mathbf{x}^S \rightarrow \mathbf{x}^{\mathrm{VR}}$ in Figure D1a). Equation (D21) shows that the stationary phase pairs (x_1^*, y_1^*), which give the travel time of the direct wave (i.e., $\phi(x_1^*, y_1^*) = r_d$), retrieve the direct downgoing wave. From equations (D10), (D14) and (D15), it is straightforward to show that there is only one stationary phase pair to create the direct wave travel time (Figure D2a). These are the two sets of primary reflections from the first boundary ($n = m = 0$, $\mathbf{x}^{\mathrm{S}} \rightarrow z_1 \rightarrow \mathbf{x}^*$ and $\mathbf{x}^* \rightarrow z_1 \rightarrow \mathbf{y}^*$, where $\mathbf{y}^* = \mathbf{x}^{\mathrm{S}}$) and the direct wave ($\mathbf{x}^{\mathrm{S}} \rightarrow \mathbf{x}^{\mathrm{VR}}$). Note that the two sets of primary reflections and any order of multiple reflections from the second boundary ($n = m, n \geq 1$) give the same

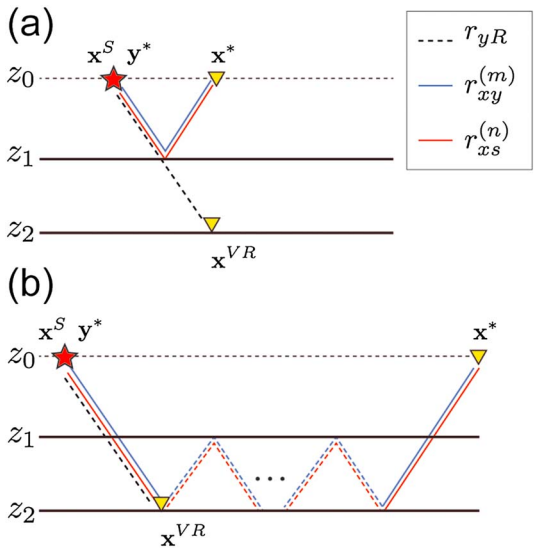

Figure D2. (a) The stationary phase pair $(\mathbf{x}^*, \mathbf{y}^*)$ which retrieves the direct downgoing wave ($n = m = 0$). r_{yR}, $r_{xy}^{(m)}$ and $r_{xs}^{(n)}$ are the travel paths required to evaluate the stationary phase contributions (see the main text for details). (b) The stationary phase pairs ($n = m$, $n \geq 1$) for the direct downgoing waves, which are excluded by the window function.

travel time (Figure D2b). These stationary phase pairs are, however, excluded due to the constraint shown in equation (D15) and removed by the window function in the retrieval process. The remaining amplitude of the retrieved direct wave is, therefore, $\tau_d'(1 - (r_1^+)^2)$.

First-order downgoing multiple reflection. Next, we check the retrieval of the first-order downgoing multiple reflection (travel path of $\mathbf{x}^S \rightarrow z_2 \rightarrow z_1 \rightarrow \mathbf{x}^{VR}$ in Figure D1a). From a discussion similar to that for the direct wave, we understand that there is only one stationary phase pair which produces the response (Figure D3a). It is the combination of the primary reflection from the second boundary ($n = 1$), the one from the first boundary ($m = 0$) and the direct wave. The other stationary phase pairs which produce the same travel time (Figure D3b) are excluded and removed during the retrieval process. The amplitude of this event is $-\tau_d'\tau_1^+\tau_1^-r_2^+r_1^+$.

Higher-order downgoing multiple reflections. It is straightforward to show that the higher-order (kth order) downgoing multiple reflections are retrieved by the following events: the primary reflection from the first boundary ($m = 0$), the multiple reflections ($n = k$), and the direct wave (Figure D4). The amplitude of this event is $-\tau_d'\tau_1^+\tau_1^-r_2^+r_1^+(r_1^-r_2^+)^{k-1}$.

In summary, the total downgoing response is written as (considering the relation $1 - (r_1^+)^2 = \tau_1^+\tau_1^-$ and $r_1^+ = -r_1^-$),

$$\hat{G}^{+,f}(\mathbf{x}^{VR}, \mathbf{x}^S, \omega) = \mu^{-1}(\mathbf{x}^S)\left(\tau_d'\tau_1^-\right)\left(\tau_1^+\hat{G}_0(r_d, \omega) + \tau_1^+r_2^+r_1^-\hat{G}_0\left(r_{(1)}, \omega\right) + \tau_1^+\left(r_2^+\right)^2\left(r_1^-\right)^2\hat{G}_0\left(r_{(2)}, \omega\right) + \ldots\right), \tag{D22}$$

where $r_{(k)}$ is the distance of propagation of the kth-order downgoing multiple reflection. The right-hand side of equation (D22) is the total downgoing wave at the virtual receiver from a surface source, scaled by the factor of $\tau_d'\tau_1^-$. The value of τ_d' is arbitrarily selected in the input direct wave. Selecting it as an inverse of the transmission response (i.e., $\tau_d' = (\tau_1^-)^{-1}$) gives the true-amplitude total downgoing wave [e.g., *Broggini et al.*, 2014].

D2. Upgoing Green's Function

In the first iteration ($k = 0$) of the retrieval of the upgoing Green's function, we have from equation (B6) the following:

$$\hat{G}^{-,f}\left(\mathbf{x}^{VR}, \mathbf{x}^S, \omega\right) = -\int_{\partial\mathbf{D}_0} d\mathbf{x}_0 \left[\hat{R}\left(\mathbf{x}^S, \mathbf{x}_0, \omega\right)\hat{G}_d^*\left(\mathbf{x}_0, \mathbf{x}^{VR}, \omega\right)\right]_{w(\mathbf{x}_0, \mathbf{x}^{VR}, -t)} + \int_{\partial\mathbf{D}_0} d\mathbf{x}_0\hat{R}\left(\mathbf{x}^S, \mathbf{x}_0, \omega\right)\hat{G}_d^*\left(\mathbf{x}_0, \mathbf{x}^{VR}, \omega\right). \tag{D23}$$

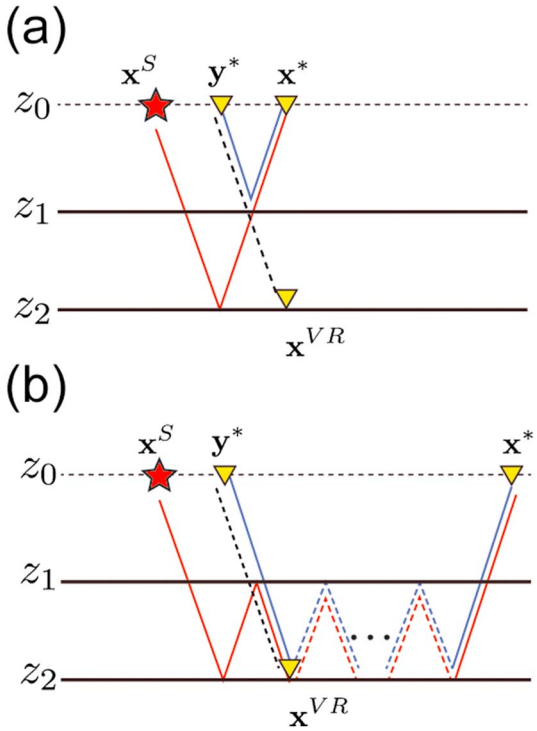

Figure D3. (a) The stationary phase pair $(\mathbf{x}^*, \mathbf{y}^*)$ which retrieves the first-order multiple downgoing waves ($m = 0$, $n = 1$). See the legend in Figure D2a for the line colors. (b) The stationary phase pairs ($m = k$, $n = k + 1$, $k > 0$) for the first-order multiple downgoing waves, which are excluded by the window function.

The two terms on the right-hand side of equation (D23) have the same form but opposite polarities. However, due to the causality of the focusing function f_1^- (see Appendix B), the first term of equation (D23) is muted for $t \geq t_d$. This implies that when we consider only the causal response, the amplitudes of the two terms before the first arrivals (t_d) cancel each other, leaving only the arrivals later than t_d. In our model, the remaining arrivals are in the part of the second term of equation (D23); these are related to the cross correlation between the reflections from the second boundary and the direct wavefield. This type of cancelation of events is extensively discussed earlier [e.g., *Wapenaar et al.*, 2012, 2014b; *Broggini et al.*, 2014]. The second term is a single spatial integral. The method of stationary phase for this type of spatial integral was applied before [*Broggini et al.*, 2014], and we do not repeat it here. The phase function of the remaining arrivals of the second term (counter part of equation (D10)) is $\phi(x_1) = r_{xs}^{(n)} - r_{xR}$. The contribution to create the primary reflection (Figure D5a) comes from the primary reflection from the second boundary and the direct wave (amplitude term is $\tau_d' \tau_1^+ \tau_1^- r_2^+$). The first- and higher-order multiple upgoing waves (Figure D5b and D5c) are retrieved from the same order of multiple upgoing waves and the direct wave (amplitude term is $\tau_d' \tau_1^+ \tau_1^- r_2^+ (r_1^- r_2^+)^k$).

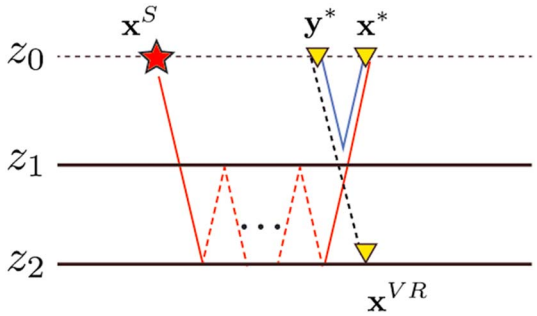

Figure D4. The stationary phase pair $(\mathbf{x}^*, \mathbf{y}^*)$ which retrieves the higher-order (kth) multiple downgoing waves ($m = 0$, $n = k$, $k > 0$). See the legend in Figure D2a for the line colors.

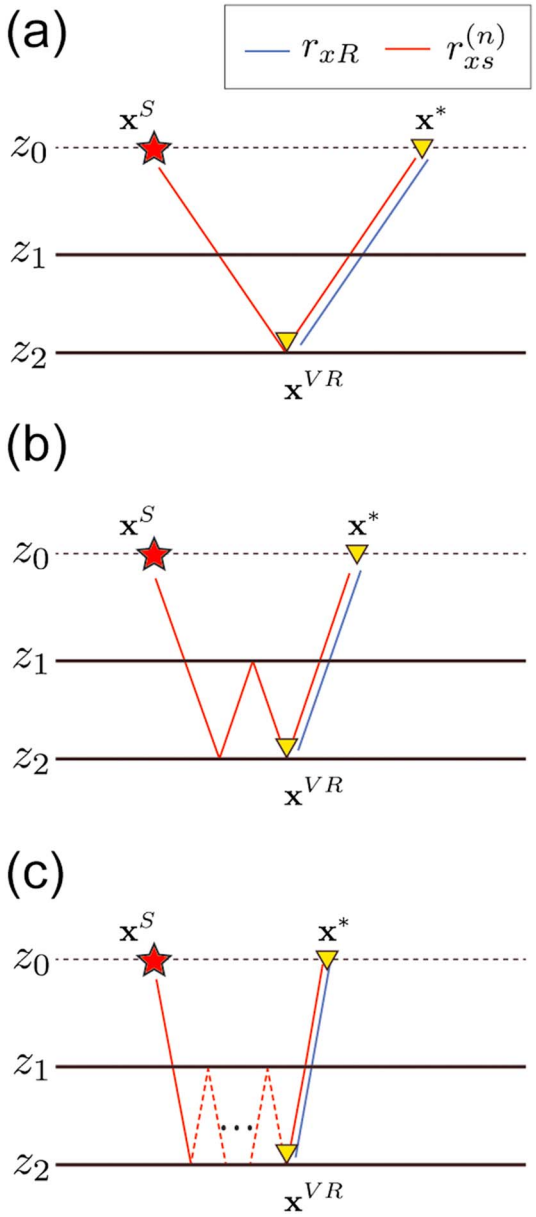

Figure D5. The stationary phase ($\mathbf{x}^*$) which retrieves (a) the primary upgoing wave ($n = 1$), (b) the first-order multiple upgoing waves ($n = 2$), and (c) the higher-order multiple upgoing waves ($n = k$, $k > 1$).

Therefore, similar to the downgoing Green's function, we obtain

$$\hat{G}^{-,f}(\mathbf{x}^{\mathrm{VR}}, \mathbf{x}^{\mathrm{S}}, \omega) = \mu^{-1}(\mathbf{x}^{\mathrm{S}}) \left(\tau_d' \tau_1^-\right) \left(\tau_1^+ r_2^+ \hat{G}_0(r_d, \omega) + \tau_1^+ (r_2^+)^2 r_1^- \hat{G}_0(r_{(1)}, \omega) + \tau_1^+ \left(r_2^+\right)^3 \left(r_1^-\right)^2 \hat{G}_0(r_{(2)}, \omega) + \ldots\right). \tag{D24}$$

This is the total upgoing Green's function scaled by $\tau_d' \tau_1^-$.

Acknowledgments
The data for this paper are available by contacting the corresponding author at s.minato-1@tudelft.nl. This work is supported by the Netherlands Research Centre for Integrated Solid Earth Science (ISES).

References

Acosta-Colon, A., L. J. Pyrak-Nolte, and D. D. Nolte (2009), Laboratory-scale study of field of view and the seismic interpretation of fracture specific stiffness, *Geophys. Prospect.*, *57*(2), 209–224.

Baik, J.-M., and R. B. Thompson (1984), Ultrasonic scattering from imperfect interfaces: A quasi-static model, *J. Nondestr. Eval.*, *4*(3–4), 177–196.

Berkhout, A., and C. Wapenaar (1993), A unified approach to acoustical reflection imaging. II: The inverse problem, *J. Acoust. Soc. Am.*, *93*(4), 2017–2023.

Broggini, F., K. Wapenaar, J. Neut, and R. Snieder (2014), Data-driven green's function retrieval and application to imaging with multidimensional deconvolution, *J. Geophys. Res. Solid Earth*, *119*, 425–441, doi:10.1002/2013JB010544.
Brown, S., and C. Scholz (1985), Closure of random elastic surfaces in contact, *J. Geophys. Res.*, *90*(B7), 5531–5545.
Chaisri, S., and E. S. Krebes (2000), Exact and approximate formulas for P-SV reflection and transmission coefficients for a nonwelded contact interface, *J. Geophys. Res.*, *105*(B12), 28,045–28,054, doi:10.1029/2000JB900296.
Chako, N. (1965), Asymptotic expansions of double and multiple integrals occurring in diffraction theory, *IMA J. Appl. Math.*, *1*(4), 372–422, doi:10.1093/imamat/1.4.372.
Choi, M. K., L. J. Pyrak-Nolte, and A. Bobet (2014), The effect of surface roughness and mixed-mode loading on the stiffness ratio K_x/K_z for fractures, *Geophysics*, *79*(5), D67–D79, doi:10.1190/geo2013-0438.1.
Conde, O. M., J. Pérez, and M. F. Cátedra (2001), Stationary phase method application for the analysis of radiation of complex 3-D conducting structures, *IEEE Trans. Antennas Propag.*, *49*(5), 724–731.
Cook, N. (1992), Natural joints in rock: Mechanical, hydraulic and seismic behaviour and properties under normal stress, *Int. J. Rock Mech. Min. Sci. Geomech. Abstr.*, *29*(3), 198–223.
da Costa Filho, C. A., M. Ravasi, A. Curtis, and G. A. Meles (2014), Elastodynamic Green's function retrieval through single-sided Marchenko inverse scattering, *Phys. Rev. E*, *90*(6), 063201.
da Costa Filho, C. A., M. Ravasi, and A. Curtis (2015), Elastic P- and S-wave autofocus imaging with primaries and internal multiples, *Geophysics*, *80*(5), S187–S202, doi:10.1190/geo2014-0512.1.
Gu, B., R. Suárez-Rivera, K. T. Nihei, and L. R. Myer (1996), Incidence of plane waves upon a fracture, *J. Geophys. Res.*, *101*(B11), 25,337–25,346.
Hopkins, D. L., N. G. Cook, and L. R. Myer (1987), Fracture stiffness and aperture as a function of applied stress and contact geometry, in *Rock Mechanics: Proceedings of the 28th U.S. Symposium, Tucson, Arizona*, edited by I. W. Farmer et al., pp. 673–680, A. A. Balkema, Rotherdam, Netherlands.
Hudson, J. A., E. Liu, and S. Crampin (1997), The mean transmission properties of a fault with imperfect facial contact, *Geophys. J. Int.*, *129*(3), 720–726, doi:10.1111/j.1365-246X.1997.tb04507.x.
Kame, N., K. Nagata, M. Nakatani, and T. Kusakabe (2014), Feasibility of acoustic monitoring of strength drop precursory to earthquake occurrence, *Earth Planets Space*, *66*(1), 1–12, doi:10.1186/1880-5981-66-41.
Knight, R., et al. (2010), Geophysics at the interface: Response of geophysical properties to solid-fluid, fluid-fluid, and solid-solid interfaces, *Rev. Geophys.*, *48*, RG4002, doi:10.1029/2007RG000242.
Li, J., H. Li, Y. Jiao, Y. Liu, X. Xia, and C. Yu (2014), Analysis for oblique wave propagation across filled joints based on thin-layer interface model, *J. Appl. Geophys.*, *102*, 39–46, doi:10.1016/j.jappgeo.2013.11.014.
Liaptsis, D., B. Drinkwater, and R. Thomas (2006), The interaction of oblique incidence ultrasound with rough, partially contacting interfaces, *Nondestr. Test. Eval.*, *21*(3–4), 109–121.
Liu, E., J. Hudson, and T. Pointer (2000), Equivalent medium representation of fractured rock, *J. Geophys. Res.*, *105*(B2), 2981–3000.
Löer, K., G. A. Meles, A. Curtis, and I. Vasconcelos (2014), Diffracted and pseudo-physical waves from spatially limited arrays using source-receiver interferometry (SRI), *Geophys. J. Int.*, *196*(2), 1043–1059, doi:10.1093/gji/ggt435.
Margetan, F., R. Thompson, and T. Gray (1988), Interfacial spring model for ultrasonic interactions with imperfect interfaces: Theory of oblique incidence and application to diffusion-bonded butt joints, *J. Nondestr. Eval.*, *7*(3–4), 131–152, doi:10.1007/BF00565998.
Minato, S., and R. Ghose (2013), Inverse scattering solution for the spatially heterogeneous compliance of a single fracture, *Geophys. J. Int.*, *195*(3), 1878–1891, doi:10.1093/gji/ggt348.
Minato, S., and R. Ghose (2014a), Imaging and characterization of a subhorizontal non-welded interface from point source elastic scattering response, *Geophys. J. Int.*, *197*(2), 1090–1095, doi:10.1093/gji/ggu037.
Minato, S., and R. Ghose (2014b), Non-linear imaging condition to image fractures as non-welded interfaces, SEG Technical Program Expanded Abstracts 2014 presented at 84th Conference of the Society of Exploration Geophysicists (SEG), pp. 3905–3909, Colo., 26–31 Oct., doi:10.1190/segam2014-0582.1.
Minato, S., and R. Ghose (2014c), Power spectral density of the heterogeneous fracture compliance from scattered elastic wavefields, *Geophysics*, *79*(2), D67–D79, doi:10.1190/geo2013-0173.1.
Minato, S., and R. Ghose (2015), Nonlinear imaging condition and the effect of source illumination: Imaging fractures as nonwelded interfaces, *Geophysics*, *80*(2), A25–A30, doi:10.1190/geo2014-0406.1.
Nagy, P. (1992), Ultrasonic classification of imperfect interfaces, *J. Nondestr. Eval.*, *11*(3–4), 127–139, doi:10.1007/BF00566404.
Nakagawa, S., K. T. Nihei, and L. R. Myer (2004), Plane wave solution for elastic wave scattering by a heterogeneous fracture, *J. Acoust. Soc. Am.*, *115*(6), 2761–2772, doi:10.1121/1.1739483.
Nam, T., T. Lee, C. Kim, K.-Y. Jhang, and N. Kim (2012), Harmonic generation of an obliquely incident ultrasonic wave in solid-solid contact interfaces, *Ultrasonics*, *52*(6), 778–783.
Nihei, K., S. Nakagawa, and L. Myer (2000), VSP fracture imaging with elastic reverse-time migration, SEG Technical Program Expanded Abstracts SEG–2000-1748 presented at 2000 SEG Annual Meeting, pp. 1748–1751, Calgary, Alberta, 6–11 Aug., doi:10.1190/1.1815759.
Oliger, A., D. D. Nolte, and L. J. Pyrak-Nolte (2003), Seismic focusing by a single planar fracture, *Geophys. Res. Lett.*, *30*(5), 1203, doi:10.1029/2002GL016264.
Pyrak-Nolte, L., and J. Morris (2000), Single fractures under normal stress: The relation between fracture specific stiffness and fluid flow, *Int. J. Rock Mech. Min. Sci.*, *37*, 245–262.
Pyrak-Nolte, L., and D. Nolte (1992), Frequency dependence of fracture stiffness, *Geophys. Res. Lett.*, *19*(3), 325–328.
Pyrak-Nolte, L., L. Myer, and N. Cook (1990), Transmission of seismic waves across single natural fractures, *J. Geophys. Res.*, *95*(B6), 8617–8638.
Pyrak-Nolte, L. J., and N. G. W. Cook (1987), Elastic interface waves along a fracture, *Geophys. Res. Lett.*, *14*(11), 1107–1110, doi:10.1029/GL014i011p01107.
Reshetnikov, A., S. Buske, and S. Shapiro (2010), Seismic imaging using microseismic events: Results from the San Andreas fault system at SAFOD, *J. Geophys. Res.*, *115*, B12324, doi:10.1029/2009JB007049.
Schoenberg, M. (1980), Elastic wave behavior across linear slip interfaces, *J. Acoust. Soc. Am.*, *68*(5), 1516–1521.
Ursin, B. (1983), Review of elastic and electromagnetic wave propagation in horizontally layered media, *Geophysics*, *48*(8), 1063–1081, doi:10.1190/1.1441529.
van der Neut, J., I. Vasconcelos, and K. Wapenaar (2014), An interferometric interpretation of Marchenko redatuming, Th-E102-11 presented at 76th Annual EAGE Meeting, Amsterdam RAI, Netherlands, 6–19 Jun.
van der Neut, J., I. Vasconcelos, and K. Wapenaar (2015), On green's function retrieval by iterative substitution of the coupled Marchenko equations, *Geophys. J. Int.*, *203*(2), 792–813.

Vasconcelos, I., K. Wapenaar, J. van der Neut, C. Thomson, and M. Ravasi (2015), Using inverse transmission matrices for Marchenko redatuming in highly complex media, SEG Technical Program Expanded Abstracts SEG–2015-5896301 presented at 2015 SEG Annual Meeting, pp. 5081–5086, New Orleans, Louisiana, 18–23 Oct., doi:10.1190/segam2015-5896301.1.

Verschuur, D. J., A. J. Berkhout, and C. P. A. Wapenaar (1992), Adaptive surface-related multiple elimination, *Geophysics*, *57*, 1166–1177, doi:10.1190/1.1443330.

Wapenaar, C., and A. Berkhout (1989), *Elastic Wave Field Extrapolation: Redatuming of Single- and Multi-Component Seismic Data*, Elsevier Sci., Amsterdam.

Wapenaar, K. (2014), Single-sided Marchenko focusing of compressional and shear waves, *Phys. Rev. E*, *90*, 063202.

Wapenaar, K., and E. Slob (2014), On the Marchenko equation for multicomponent single-sided reflection data, *Geophys. J. Int.*, *199*(3), 1367–1371, doi:10.1093/gji/ggu313.

Wapenaar, K., E. Slob, and R. Snieder (2008), Seismic and electromagnetic controlled-source interferometry in dissipative media, *Geophys. Prospect.*, *56*(3), 419–434.

Wapenaar, K., F. Broggini, and R. Snieder (2012), Creating a virtual source inside a medium from reflection data: Heuristic derivation and stationary-phase analysis, *Geophys. J. Int.*, *190*(2), 1020–1024, doi:10.1111/j.1365-246X.2012.05551.x.

Wapenaar, K., J. Thorbecke, J. van der Neut, F. Broggini, E. Slob, and R. Snieder (2014a), Green's function retrieval from reflection data, in absence of a receiver at the virtual source position, *J. Acoust. Soc. Am.*, *135*(5), 2487–2861.

Wapenaar, K., J. Thorbecke, J. van der Neut, F. Broggini, E. Slob, and R. Snieder (2014b), Marchenko imaging, *Geophysics*, *79*(3), WA39–WA57, doi:10.1190/geo2013-0302.1.

Woodhouse, J. H. (1974), Surface waves in a laterally varying layered structure, *Geophys. J. Int.*, *37*(3), 461–490.

Worthington, M., and R. Lubbe (2007), The scaling of fracture compliance, *Geol. Soc. London Spec. Publ.*, *270*(1), 73–82.

Worthington, M. H., and J. A. Hudson (2000), Fault properties from seismic Q, *Geophys. J. Int.*, *143*(3), 937–944, doi:10.1046/j.1365-246X.2000.00315.x.